Optimal stimulation waveform for efficacious high frequency block of the pudendal nerve with minimized electrochemical damage.

A Computer Simulation Optimization Approach

Gerard Baquer Gómez

OPTIMAL STIMULATION WAVEFORM FOR EFFICACIOUS HIGH FREQUENCY BLOCK OF THE PUDENDAL NERVE WITH MINIMIZED ELECTROCHEMICAL DAMAGE.

A COMPUTER SIMULATION OPTIMIZATION APPROACH

by

Gerard BAQUER GÓMEZ

to obtain the degree of Master of Science in Microelectronics
at the Delft University of Technology,
to be defended publicly on Monday September 18th, 2018

Student number:	4625080
Project duration:	January 8th, 2018 - September 12th, 2018
Thesis committee:	dr. ir. W. A. Serdijn, TU Delft, supervisor
	dr. ir. R.F. Remis, TU Delft
	dr. V. Valente, TU Delft
	dr. M. Negrello, Erasmus MC, external expert

An electronic version of this thesis is available at http://repository.tudelft.nl/.

Dedicated to Daniel Escobar Solà.

ACKNOWLEDGEMENTS

Gerard Baquer Gómez
September 2018

I would like to start by expressing my most sincere gratitude to my supervisor, Dr. Wouter Serdijn, for his amazing job in guiding and supporting my work. Not only has he been of crucial help from an academic perspective but my conversations with him inspired me in choosing my next career step. By backing up my application he helped me obtain my Ph.D. position and secure funding for it.

I fondly appreciate the help offered by Dr. Bertil Blok in providing a strong medical background during the early stages of this thesis. A special thanks goes to Dr. Virgilio Valente for his support and honest feedback.

I also take the opportunity to thank Dr. Rob Remis and Dr. Mario Negrello for agreeing to be part of my MSc thesis committee.

Being part of the Bioelectronics group has been an amazing and inspiring experience. It is a lively group formed by many incredible researchers of exceptional personal quality. I would like to especially thank Amit, Federico, Thasos and the rest of the students in the MSc room.

I want to thank Robbert Eggermont, from the Intelligent Systems group, for granting me access to their powerful server network where all the simulations of this thesis were run.

These two years have been an amazing learning experience and I would like to thank every professor and fellow student who challenged me, advised me, helped me in difficult times and inspired me with their work. You all helped me become a better professional.

My extreme gratitude goes to Deniz, Guille, Ashish and Raoul who made me feel at home away from home; Selina and Ahmed, who were always there; and Rosario, a good friend.

A special mention goes to all those waiting for me at home, an immense source of motivation during hard times.

Finally, I would want to close by manifesting my most sincere gratefulness to my family, the cornerstone of my being. My parents, Eva and Javi, two complementary role models who have always shown their unconditional support in all of the challenges embraced in my life. My brother, Albert, a pupil that has ended up surpassing the master, a human being I still have a lot to learn from. And her, Maria, a person with a contagious passion for life who continues to pull me to higher goals.

CONTENTS

ABSTRACT

The use of high-frequency stimulation for conduction block of the pudendal nerve has potentially high benefits for patients suffering from non-neurogenic urinary retention [1]. Special care has to be put in the design of stimulation parameters to ensure safe operation and prevent electrode and tissue damage [2]. While high-frequency conduction block has been studied and used for many years, only standard waveforms, such as charge balanced sinewaves and square waves, have been utilized. Several studies have anticipated that the use of non-standard, non-symmetrical and slightly charge unbalanced waveforms may provide electrochemically safer stimulation protocols [3].

In this computational simulation study, the MRG model is combined with an electrode-tissue interface (ETI) model based on in vivo experimental data to create a computational model capable of assessing both the efficacy and electrochemical safety of any given stimulation waveform. This model is coupled to a differential evolution algorithm to find the optimal waveform parameters that ensure a successful conduction block and a minimized charge injection through irreversible faradaic reactions.

The classical DE algorithm is adapted to include several improvements such as evolutionary adaptive parametrization, elitism, and variable pattern to increase its performance. Additionally, acknowledging the fact that the axonal model is the main bottleneck in computational terms, an improvement baptized as "model down-sampling" is presented. Model down-sampling consists on only executing the axonal model to determine the effectiveness of the block once every N generations. This modification manages to double the execution speed without compromising accuracy.

The results show that non-standard waveforms with a slight charge imbalance keep the ETI voltage well within the narrow electrochemical safe window of -0.25V and 0.55V, thus avoiding any irreversible charge injection process. The obtained waveforms show a 39.8% improvement on the safety margin with respect to the best performing standard stimulation waveform. The obtained results prove that well designed non-standard waveforms can lead to electrochemically safer high-frequency stimulation.

Keywords: High-frequency stimulation, modeling, optimization, safety, blocking, nerve conduction block, differential evolution, pudendal nerve.

1

INTRODUCTION

1.1. PROBLEM STATEMENT

Millions of people have difficulty in emptying their urinary bladder, and given its close correlation with age, the problem will grow exponentially with the aging population [4]. The symptoms of this condition include straining to void, voiding difficulty with a sensation of incomplete emptying and increased post-void residual urine volume [5].

Many conditions affecting the nervous system such as spinal chord injury or multiple sclerosis can be behind this condition but causes can also be non-neurogenic. For instance, the urinary retention condition has been correlated with aging as nerve control tends to degenerate, detrusor is demeaned and bladder outlet is obstructed [5]. Diabetes mellitus can also produce bladder damage. A minor proportion of these cases are iatrogenic, such as pelvic surgery related nerve injury [6, 7] or drug-related bladder contractile dysfunction [8]. In addition, many more non-neurological patients suffer from similar problems without an obvious cause.

In the treatment of non-neurogenic urinary retention, to circumvent the detrimental effects of classical treatments available, such as rhizotomy, catheterization or pharmacology, the use of alternative treatments based on electrical stimulation has gained a high research interest. Electrical stimulation acts quickly, reverses rapidly and has a higher selectivity [9]. Several studies have successfully targeted different nervous structures involved in the micturition reflex such as the Sacral Root or the Pontine Micturition Center [1, 10]. The main problem with these approaches is that the implantation surgery involved is highly invasive given the internal location of the structures chosen. Additionally, given the diversity of the organs affected by the targeted structures, these approaches have reported a reduced selectivity showing side effects in other regions of the urinary system.

Stimulation of the pudendal nerve can solve both these issues given that its location requires a less invasive implantation surgery and its stimulation leads to fewer side effects given the reduced number of regions innervated by it. By means of high-frequency stimulation of the pudendal nerve, the spikes transmitted by the pudendal nerve can be blocked, which will in turn cause relaxation of the sphincter and voiding.

While high-frequency conduction block has been studied and used for many years, only standard waveforms, such as charge balanced sinewaves and square waves, have been utilized. Several studies have anticipated that the use of non-standard, non-symmetrical and slightly charge unbalanced waveforms may provide electrochemically safer stimulation protocols [3]. We aim to determine the optimal waveform to reduce the electrochemical damage to a minimum while ensuring the efficacy of the conduction block.

In order to do so, we propose the creation of a computational model capable of assessing the efficacy and the electrochemical safety of a given stimulation waveform. The model will then be coupled to a computer optimization algorithm to find the desired optimal waveform.

1.2. STATE OF THE ART

Several simulation studies have been conducted to optimize different stimulation parameters using computational optimization techniques. The range of techniques used is wide and includes: genetic algorithms (GAs) [11–14], particle swarm optimization [15] and artificial neural networks [16].

Most of the research in the field of computer optimization of neural stimulation focuses on deep brain stimulation (DBS) applications. Peña et al. 2017 [15] studied the optimal electrode configuration and stimulation amplitude to increase effectiveness (maximize activation in regions of interest and minimize activation in regions of avoidance) and minimize power consumption. In order to do that they relied on a computer 3D FEM model of the area of interest of the brain and a linear simplification of the membrane model that only determined if activation occurred or not. A particle swarm optimization algorithm (PSO) was used for the optimization. Several particles explored the 32-dimensional space formed by the stimulation amplitude in each of the electrodes.

In order to increase the efficiency of brain stimulation in treating Parkinson's and reduce the energy required, Brocker et al. 2017. [14] used a genetic algorithm to find the optimal stimulation pattern. Efficiency was quantified using the error index, the ratio between the total number of errors (misses, bursts or spurious) and the total number of stimulation pulses. The model used was a block diagram with weighted inhibitory and excitatory connections of the basal ganglia. The resulting optimal pattern had an average frequency of 45 Hz and reduced the EI in the model by almost 98% relative to a 45-Hz, constant-frequency stimulation. In a similar fashion, Cassar et al. 2017 [3], developed a genetic algorithm for two different DBS applications. In a basal ganglia model, the optimal temporal pattern was found that minimized signal power in the beta frequency band and average stimulation frequency. In a dorsal horn model, they minimized the average firing rate as well as the average stimulation frequency. The standard GA found patterns that outperformed fixed-frequency, clinically-standard patterns in biophysically-based models of neural stimulation, but the modified GA, in many fewer iterations, consistently converged to higher-scoring, non-regular patterns of stimulation.

Probably the closest work to this thesis is Wongsarnpigoon et. al. 2010 [12]. In the pursuit of an energy-optimal waveform shape for neural stimulation, a genetic algorithm was used to optimize the waveform shape. They used the MRG model, a computational model of extracellular stimulation of a mammalian myelinated axon. Each waveform in the population was represented by several genes that represented the amplitude of

the signal in every timestep. A total of 50 stimulation waveforms were randomly generated and evaluated in a cost function that consisted of the sum of the energy consumed by the waveform (E) and a substantial penalty if the waveform failed to elicit an action potential. After each generation, the top 10 fittest waveforms remain and 40 new waveforms are generated by crossing over two randomly selected parents and mutating every gene by scaling by a factor of 1 with a standard deviation of 0.025. The outcome of these simulations was a set of waveform shapes that were more energy efficient than many conventional waveforms used in neural stimulation.

In conclusion, computer optimization techniques, and in particular stochastic swarm intelligence techniques such as PSO, GA, and NN, are a powerful tool to foster the research in neural stimulation waveform optimization given its demonstrated effectiveness and results. While each of the available studies focuses on optimizing different aspects of neural stimulation, they focus exclusively on action potential elicitation by means of low-frequency stimulation. The field of high-frequency nerve conduction block can potentially benefit from these techniques to exploit the anticipated beneficial effects that the use of non-standard, non-symmetrical and slightly charge unbalanced waveforms can have on electrochemical safety [17].

1.3. PROPOSED METHOD: COMPUTATIONAL MODEL COUPLED WITH AN OPTIMIZATION ALGORITHM

We propose the combination of an axonal model and an electrode-tissue interface (ETI) model to create a computational model capable of assessing the efficacy of the conduction block as well as its electrochemical safety. The parametrization of the model will take into account the anatomical and physiological characteristics of the pudendal nerve. This model will be coupled to an optimization algorithm to find the optimal stimulation waveform for efficacious high-frequency block of the pudendal nerve with minimized electrochemical safety.

The computational models needed are highly complex and show nonlinear characteristics that render classical optimization techniques infeasible. A stochastic computer optimization technique will be used as it provides a computationally efficient way of optimizing such models. To further decrease the computation time burden, parallel programming will be employed.

1.4. OUTLINE OF CHAPTERS

Chapter 1 introduced the goal of finding the optimal waveform parameters to ensure electrochemical safety in high-frequency conduction block of the pudendal nerve. Similar studies available in literature were reviewed and the proposed methodology was presented.

Chapter 2 provides a theoretical framework of urinary retention and its treatment. Special stress will be put on reviewing the high-frequency stimulation parameters used in previous clinical and simulation studies.

Chapter 3 presents the ETI model, the first of the three main components of this simulation study, which is used to assess electrochemical safety. Initially, relevant safety

considerations are reviewed. Later, the concept of Electrode Tissue Interface is introduced and extensively studied. The chosen experimentally parametrized ETI model is exposed and several standard stimulation schemes are evaluated to clearly understand how each waveform parameter influences electrochemical safety.

Chapter 4 presents the McIntyre, Richardson, and Grill (MRG) nerve axonal model, the second key component of this simulation study which is used to determine the efficacy of the nerve conduction block. Initially, the available computational models are presented. Later a more detailed description of the chosen model is offered. Finally, the implementation of the model is briefly discussed.

Chapter 5 describes the design of the Differential Evolution algorithm, the third and last piece of this simulation study, used in Chapter 6 to find the optimal stimulation waveform pattern. The different optimization algorithm alternatives are presented and compared and Differential Evolution is selected based on a suitability comparison. Later several improvements to the algorithm are proposed and analyzed.

Chapter 6 presents the resulting optimal waveform that achieves an electrochemically optimally safe nerve conduction block.

Finally, chapter 7 summarizes the main contributions of this work and outlines several directions for future work.

2

URINARY RETENTION AND TREATMENT

In this chapter, we provide the basic theoretical framework of this thesis. In the first section, non-neurogenic urinary retention is explained along with the available treatments highlighting high-frequency block as a promising option. Later, a short study of the anatomy and physiology of the pudendal nerve is conducted to elicit requirements for the computer model described in Chapter 4. In a later section, key electro-physiological and technical aspects of electrical nerve stimulation will be discussed with special stress on high-frequency stimulation. Finally, a picture of the state-of-the-art in nerve conduction block parameters will be depicted with the intention of motivating the need for exploring non-standard waveforms.

2.1. NON-NEUROGENIC URINARY RETENTION

Millions of people have difficulty in emptying their urinary bladder and given its close correlation with age the problem will grow exponentially with the aging population [4]. The symptoms of this condition include straining to void, voiding difficulty with the sensation of incomplete emptying, increased post-void residual urine volume [5]. In this section, we will try to get a global understanding of the mechanisms involved in this medical condition. We will start by reviewing the anatomy and physiology of the micturition reflex. Later, the pros and cons of the available treatments today will be presented in order to motivate the need for the approach proposed.

2.1.1. ANATOMY AND PHYSIOLOGY OF THE MICTURITION REFLEX

In order to understand the possible causes and potential treatments of urinary retention, a basic comprehension of the micturition reflex is needed. Figure 2.1 shows the basic anatomical structures responsible for this reflex while Figure 2.2 shows the physiological dependencies between them. Micturition, also called urination or voiding, is the act of emptying the urinary bladder. For micturition to occur, three things must hap-

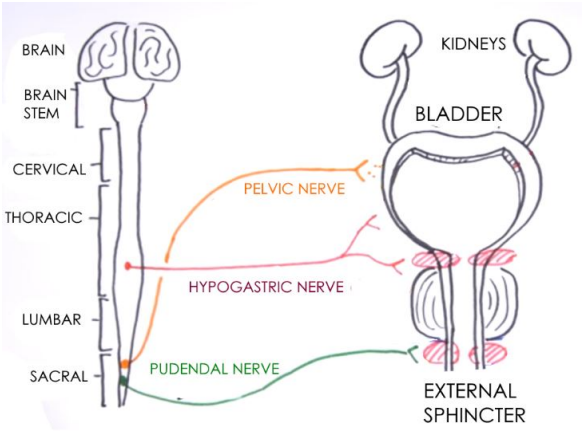

Figure 2.1: Main anatomical structures of the urinary system [18]

pen simultaneously: (1) the bladder must contract, (2) the internal urethral sphincter must open, and (3) the external urethral sphincter must open. The detrusor muscle (responsible for contracting the bladder) and its internal urethral sphincter are composed of smooth muscle and are innervated by two efferent nerves: the pelvic nerve (causing contraction) and the hypogastric nerve (responsible for relaxation). In addition, the detrusor walls have stretch receptors connected to afferent fibers which measure the pressure and volume of the bladder. The external urethral sphincter, on the other hand, is a skeletal muscle which is constantly being stimulated through the pudendal nerve to sustain its contraction. The firing rate can be voluntarily be lowered causing the muscle to relax. The control of the micturition reflex is complex and falls out of the scope of this thesis but it is important to know that it is mediated at two different levels: (1) at an involuntary reflex level at the sacral region of the spinal cord and (2) at the brainstem (pontine storage center which inhibits micturition and pontine micturition center which promotes the reflex)[18].

From this basic understanding of the micturition reflex, one can easily infer the three main general prerequisites for proper micturition: low bladder outlet resistance, good bladder contractility, intact reflex neural pathways. When any of these prerequisites are not met voiding dysfunction may occur [5]. Causes can stem from a neural injury or disease, cerebral stroke [19], Parkinson's disease [8], multiple sclerosis [20], peripheral neuropathy or spinal chord injury. Extensive research is being conducted on the treatment of neurogenic urinary retention.

Nevertheless, causes can also be non-neurogenic. For instance, urinary retention condition has been correlated with aging as nerve control tends to degenerate, detrusor is demeaned and bladder outlet is obstructed [5]. Diabetes mellitus can also produce bladder damage. A minor proportion of these cases are iatrogenic, such as pelvic surgery related nerve injury [6, 7] or drug-related bladder contractile dysfunction [8]. In addition, many more non-neurological patients suffer from similar problems without an obvious cause.

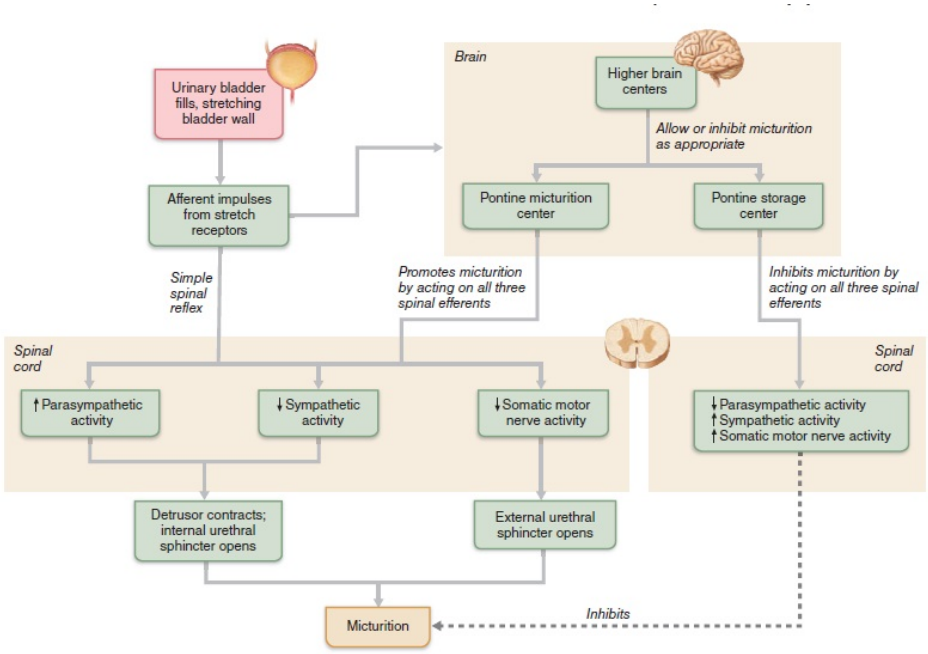

Figure 2.2: Diagram representing the phisiological dependencies between the main anatomical structures involved in the control of the micturition reflex [18]

In this thesis, we will focus on treating cases of urinary retention with non-neurogenic causes, where the nervous pathways involved in the micturition reflex are not damaged.

2.1.2. CONVENTIONAL TREATMENT

The most common treatment for urinary retention is to mechanically empty the bladder with catheterization [21]. This solution results in infections, pain and excessive health-care costs. Catheters are associated with blockage, dislodgement, bleeding, strictures, stones, leakages, and other complications that greatly affect the quality of life [22]. The complications can lead to emergency-room visits, hospitalization, and life-threatening situations. They, also, lead to embarrassment and even admission into nursing homes.

Another proposed treatment is the injection of botulinum toxin to the external sphincter which causes relaxation, thus reducing bladder outlet resistance. Alternatively, surgical procedures have also been proposed but always regarded as the last option due to its invasive essence, high expenses and irreversible effects [5].

Pharmacology offers a less physically invasive alternative. The intake of specific compounds can directly stimulate or inhibit specific neuron receptors to induce bladder contraction and external sphincter relaxation [23]. Alternatively, the application of pressure or temperature [24] could also lead to similar effects. The main problem with these approaches stems from their limited temporal and spatial control.

2.1.3. TREATMENT USING HIGH-FREQUENCY ELECTRICAL STIMULATION

Electrical stimulation acts quickly, reverses rapidly and has a higher selectivity [9], which makes it the perfect candidate for the treatment of non-neurogenic urinary retention. The golden standard is the use of high-frequency stimulation which is the focus of this work and will be discussed in depth in the next section. An alternative approach to high-frequency stimulation is the use of direct currents (DC). This method has proven to be rapid, effective, reversible and localized but the large injection of charge into the tissue involved, limits its application to really short periods of time and large electrodes with a high charge accumulation capacity are required [23].

Several studies have successfully targeted different nervous structures involved in the micturition reflex such as the Sacral Root [1] or the Pontine Micturition Center [10]. Given the complicated access to these locations, the surgical procedures needed are highly invasive, especially in the case of the pontine micturition center which requires the use of deep brain stimulation (DBS). Additionally, given the complex nature of these structures, side effects such as numbness or pain in parts of the urinary system other than the external sphincter have been reported in previous studies.

As an alternative, one can use high-frequency stimulation to block the pudendal nerve and cause relaxation of the sphincter. The main advantage is the less invasive surgery needed. Additionally, given the more distal location of stimulation, a more localized and targeted treatment can be expected.

2.2. ANATOMY AND PHYSIOLOGY OF THE PUDENDAL NERVE

The pudendal nerve originates in the lumbosacral plexus (L4-S4). Its fibers are 80% sensory fibers and 20% motor fibers. Inside the pudendal canal, the nerve branches into 3

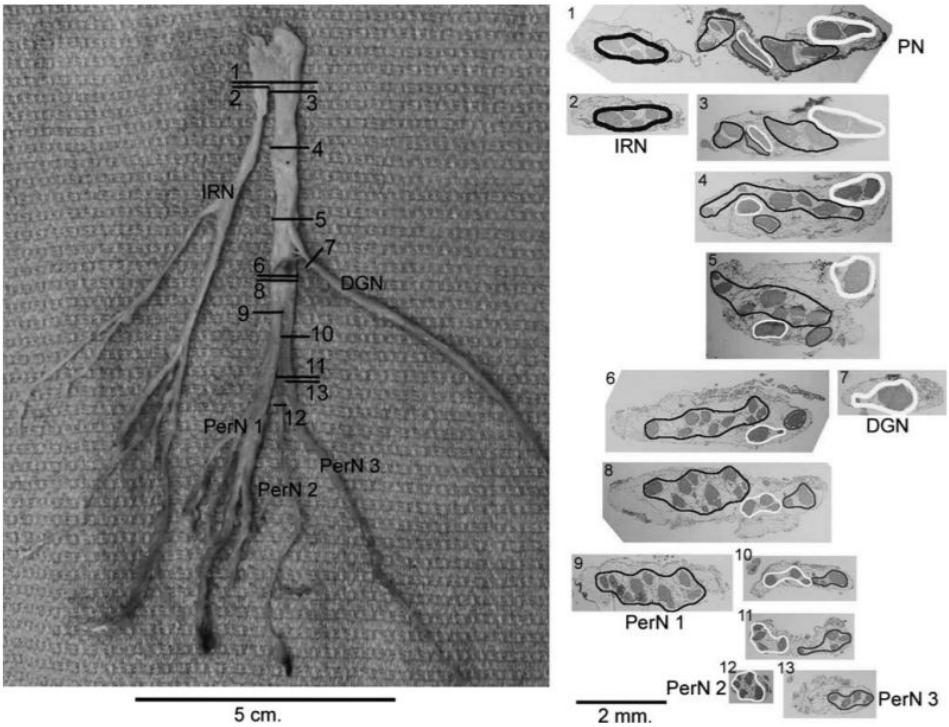

Figure 2.3: Cross-sectional fascicular anatomy of the pudendal nerve. (Left) Pudendal nerve with major branches (DGN, IRN, PerN) and cross-sections shown in the right. (Right) Fascicle map [27]

smaller nerves [18, 25]:

1. Inferior Rectal Nerve (IRN): rectum, anal canal, peri-anal skin, and external anal sphincter.

2. Perineal Nerve (PerN): perineum, vagina, urethra, male scrotum, labia, transverse perineal muscle, and urethral sphincter.

3. Dorsal Genital Nerve (DGN): skin of the clitoris/penis, bulbocavernosus, and ischiocavernosus muscles.

Several anatomical studies conclude that, when traversing the pudendal canal, the pudendal nerve has a relatively flat, elliptical cross-section with an effective diameter of 3.2mm ($\sigma = 0.56mm$), a major axis of 4.3mm ($\sigma = 0.9mm$) and a minor axis of 1.7 mm ($\sigma = 0.45mm$) [26, 27]. It contains dozens of small individual fascicles (effective diameter between 100 and 350 μm). As most long nerve fibers in the PNS, the fibers within the pudendal nerve are myelinated [18]. Figure 2.3 shows a picture of the cross-sectional fascicular anatomy of the pudendal nerve.

2.3. UNDERSTANDING HIGH-FREQUENCY NERVE CONDUCTION BLOCK

2.3.1. ELECTRO-PHYSIOLOGICAL ASPECTS OF NERVE CELLS

The nerve cell is usually divided into three main parts: the soma (containing the nucleus), numerous fibers stemming from the soma refered to as the dendrites and a long fiber called the axon. Signals are usually generated at the soma, propagated down the axon and transferred to the dendrites of neighboring cells. These signal paths allow nerve cells to communicate with each other [18].

The membrane voltage (V_m) is a crucial magnitude to model and understand this process from an electrical perspective. This magnitude is defined as the potential difference between the outer surface (Θ_o) and the inner surface (Θ_i) of the membrane. This difference in potential is mainly due to the different concentrations of ions inside and outside of the cell [28].

By means of electrical stimulation, the membrane potential can be altered. If a nerve cell is stimulated, the membrane voltage changes. An excitatory or depolarizing stimulus leads to an increase of the membrane potential while an inhibitory or hyperpolarizing stimulus implies a decrease. If the excitatory stimulus is strong enough to surpass the threshold voltage (V_{th}) the membrane produces an action potential. The action potential has the same characteristics independently of the magnitude of the stimulus, which is why the action potential is usually described as an all-or-nothing response. Figure 2.4 shows the evolution of an action potential.

It is important to note that in peripheral nerves, the refractory period ranges between 0.7 and 2 ms, which limits the maximum firing between 500 and 1400 spks/s [29]. This can serve as a base measure to understand, in general terms, why the frequencies capable of inducing a nerve conduction block are in the order of the kHz.

The conduction velocity of an action potential depends on factors such as maximum ion conductance, membrane capacitance, medium resistivity, and threshold voltage. Additionally, in myelinated axons (surrounded by myelin sheath) action potentials can only be generated in the so-called nodes of Ranvier. The presence of these nodes creates a saltatory conduction which increases dramatically the conduction velocity.

In order to understand the formation of an action potential, it is necessary to understand the key role that ion concentrations play in the membrane potential. The main ions responsible for the changes in the membrane potential are potassium (K+), sodium (Na+), and chloride (Cl-). The movement of ions between the inside and the outside of the membrane is mediated by two main forces: diffusional forces (ions flow from high to low concentration) and electric-field forces. The Goldman-Hodgkin-Katz equation combines the influence of all these forces to determine the membrane voltage[28]. The resting voltage of a nerve cell is reached when all of these forces even out.

The permeability of the membrane is different for every ion and it is sensitive to the membrane voltage among other factors. The first attempt to model the membrane behavior was conducted by Hodgkin and Huxley who developed a mathematical model to fit their voltage-clamp experimental data on a squid's axonal membrane [31]. The Hodgkin and Huxley model is still one of the standards used in state-of-the-art research today but several alternative models have been proposed through the years to include

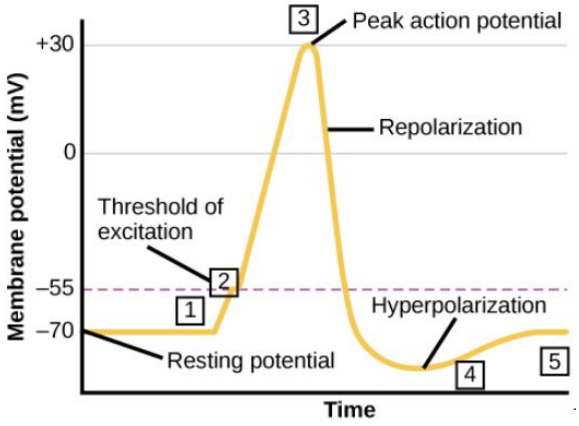

Figure 2.4: Time response of an action potential [30] (1) A stimulus from a sensory cell, another neuron or an electrode causes the target cell to depolarize toward the threshold potential. (2) If the threshold of excitation is reached, all Na+ channels open and the membrane depolarizes. (3) At the peak action potential, K+ channels open and K+ begins to leave the cell. At the same time, Na+ channels close. (4) The membrane becomes hyperpolarized as K+ ions continue to leave the cell. The hyperpolarized membrane is in a refractory period and cannot fire. (5) The K+ channels close and the Na+/K+ pump restores the resting potential.

more complex aspects: FH [32], CRRSS [33], SRB [34] and MRG [35]. A more in-depth analysis and comparison of the different models will be presented in Chapter 4

2.3.2. ELECTRO-PHYSIOLOGICAL ASPECTS OF HIGH-FREQUENCY BLOCK

Kilohertz-frequency stimulation (KHF, KES or KHFAC) can achieve different neural responses depending on parameters such as signal amplitude, distance to the electrode, electrode geometry, frequency or stimulation waveform [36–39]. In wide terms, the effects can be classified into two main categories: KHF stimulation may elicit neural activity or it may lead to a conduction block. KHF block can be further divided into two types. On the one hand, we have nerve conduction block where the conduction of action potentials is interrupted under the blocking electrode. Another type of block is neurotransmitter depletion block, where action potentials are generated at such a high frequency (typically above 100Hz) that the neurotransmitters at the synapse or neuromuscular junction are temporarily depleted causing a temporary block [17]. In this study, we investigate the safety of nerve conduction block.

While the available studies tend to disagree in the ranges of frequencies, amplitudes, and effects achieved, the vast majority of studies on high-frequency block agree on a few premises that can be safely taken as base knowledge for our study. It has been demonstrated that KHF block acts quickly, reverses rapidly, requires lower amplitudes for larger diameter fibers, requires higher amplitudes for higher frequencies and it is accompanied by an initial activation referred to as the onset activation [9].

The duration and number of action potentials elicited in the onset response depend on the stimulation parameters. It is relevant to highlight that the onset response is not desired and can be a significant clinical impediment as it leads to muscle contraction

and pain. Several studies have tried to eliminate or mitigate the onset response. The initial approach of slowly ramping up amplitude has been proven ineffective [40]. It has been demonstrated that large amplitudes [41], higher frequencies (>20kHz) [42] and improved electrode geometry [43] can shorten the duration of the onset response. Additionally, it has been proven that it is possible to, once the block has already been established, modulate the KHF waveform (amplitude or frequency) between the blocking and non-blocking operation regions without producing any additional onset responses [41, 44]. As an alternative, the use of DC electrodes is a successful way of blocking the onset firing generated by the KHF signal. A similar approach relies on charge imbalanced waveforms to induce the desired DC offset. The main problem with the DC block approach is that it has to be held for periods of up to 5 seconds which, in spite of the small currents required (around 2mA) is long enough to cause irreversible damage [17]. As a solution, the design of high-charge capacity electrodes for the DC block has been proposed.

While the reversibility of KHFAC has been shown to be instantaneous, under certain conditions it has been shown to relate to a "carry-over" effect, an extended period of time where the block is maintained after turning the blocking stimulation off. Three different types of recovery have been identified[45]. "Instantaneous recovery" is the most common case and conduction is recovered between 0-3s. This type of recovery takes place if the duration of the KFHAC block is less than 15 min. When such stimulation is applied for a longer time span "fast recovery" is observed, associated with carry-over times of less than 3 min. Finally, if the stimulation is applied for longer periods than 40 minutes the carry-over can last up to 2 hours. The exact mechanisms behind the carry-over effect are not well understood but the most extended theories indicate that it is likely caused by a temporary local depletion of the metabolites needed for nervous conduction [17]. The blocking of the pudendal nerve is an acute stimulation that will not exceed the "fast-recovery" limit and it can be reliably stated that instantaneous recovery will occur.

The underlying mechanisms responsible for high-frequency block are still not well understood and three key explanations coexist in literature. One of the initial explanations attributed the responsibility of the conduction block to the accumulation of extracellular potassium [46], which has been recently discarded as the main cause given the reported high speed at which the block takes place [42]. An alternative explanation claims that the inward sodium currents are overwhelmed by the outward sodium currents at the nodes of Ranvier [47, 48]. This theory is based on HH and FH simulations and is still lacking an experimental confirmation. Finally, the third and most widespread explanation is based on the inactivation of sodium channels block. During KHF there is a membrane depolarization which causes an inactivation of 90% of the sodium channels in the nodes close to the blocking electrode [49–51].

2.4. WAVEFORM AND STIMULATION PARAMETERS FOR PUDENDAL NERVE BLOCKAGE

The efficacy of the high-frequency block is tightly related to the choice of waveform parameters. The lowest frequency reported is 1kHz in a clinical study on a cat pudendal nerve [52] but most studies establish this lower limit between 3 and 5kHz [53]. Fre-

quencies as high as 70kHz have been demonstrated to be effective in a full conduction block of peripheral nerves experimentally [54] and simulation studies have shown that frequencies of up to 300kHz can be used [55]. The standard measure to compare different studies is the block threshold, defined as the minimum signal amplitude needed to successfully achieve a full conduction block. Block threshold values depend on the waveform used. Most of the available studies focus on square waves or sinewaves and it has been reported that the block threshold needed for square waves is lower given their increased charge per phase [23]. It has been demonstrated that asymmetrical patterns can be more effective [56] and it is predicted that the use of non-standard and charge unbalanced patterns can further improve effectiveness [17].

The type of axon (myelinated or unmyelinated), as well as its diameter, have shown to have an influence on block threshold values. In general terms, smaller axon diameters require higher threshold values. Unmyelinated axons present higher threshold values. Additionally, the block threshold has been demonstrated to follow a linear monotonic increase with frequency in the case of myelinated large fibers and a non-monotonical relationship for unmyelinated and small fibers [23].

2.5. CONCLUSION

In this chapter, we have provided a physiological and anatomical overview of the micturition reflex to introduce the possible causes and treatments of urinary retention. The project focuses on the treatment of non-neurogenic cases where the neurological pathways are intact. Out of all available treatment options, electrical stimulation stands out as a fast, reliable, safe and highly selective option. In particular we will focus on high frequency-conduction block of the pudendal nerve.

In its pass through the pudendal canal, the pudendal nerve has an elliptical cross-section with an effective diameter of $3.2mm$, it contains dozens of fascicles which are composed of several myelinated axons with diameters as small as 5 μm. These parameters are used as requirements for the modeling presented in Chapter 4.

Additionally, the main physiological aspects of nerve cell stimulation have been reviewed with a special focus on high-frequency nerve conduction block. Aspects such as signal amplitude, frequency, waveform, and electrode configuration have proven to influence the efficaciousness of the high-frequency block and the available studies tend to disagree in these parameters. All studies agree on high-frequency block being quick acting and rapidly reversible. Additionally, it requires lower amplitudes for larger diameter fibers and higher amplitudes for higher frequencies. Another particularity of high-frequency block is the phenomenon of onset activation, a temporary firing activity before a complete block is achieved.

Finally, a review of the current state of the art in the waveforms and parameters used in high-frequency block of pudendal nerve has been presented. The available studies focus on completely charge balanced sinewaves and square waves. Asymmetrical, charge imbalanced and non-standard patterns can potentially lead to more effective stimulation.

3

MODELLING ELECTROCHEMICAL SAFETY OF HIGH-FREQUENCY NERVE STIMULATION

In this chapter, we explore the computational model used to assess the electrochemical safety of high-frequency stimulation. The first section reviews general safety considerations to be taken into account from an electrical perspective. In the second section, we analyze the electrode-tissue interface explaining its importance in assessing the safety of electrical stimulation and reviewing the most commonly used models. Later, the choice of the proper ETI model is motivated and the chosen model is described in detail. We conclude the section by analyzing the ETI voltage response of the most widely spread high-frequency stimulation paradigms. Finally, a conclusion is presented summarizing the key points regarding electrochemical safety and its modeling.

3.1. ELECTRICAL SAFETY CONSIDERATIONS

In general terms, the potential damages associated with electrical stimulation can be divided into two main sections: passive damage is associated with implantation and presence of the device in the tissue and dynamic damage is associated with electrical stimulation. Passive causes include mechanically induced damage associated with implantation, use or removal as well as body rejection of the device. Dynamic causes mainly include heat generation and electrically induced causes. In this section, we will focus on the electrical mechanisms of damage and the consequent safety considerations [57].

3.1.1. SHORT-TERM CONSIDERATIONS

HYPER-ACTIVATION

A close correlation has been found between axon damage and its activation frequency and intensity. When activated more frequently and strongly axons suffer more damage [58]. Neuronal damage stems from the hyper-activation of neurons [59]. The increased

frequency of activation can lead to detrimental changes in the local environment such as depletion of oxygen and glucose as well as alterations in the intracellular and extracellular ionic concentrations [60]. Some have stated that neural hyperactivity might be much more of a crucial factor in causing neural damage than previously anticipated [61]. More research is needed in this direction to further understand the mechanisms of tissue damage. A standard practice to prevent hyper-activation relies on the choice of sufficiently low stimulation parameters.

ELECTROPORATION

The phenomenon of electroporation is another damage mechanism associated with electrical stimulation. Given sufficiently high stimulation parameters, the electric field can reach strength levels that lead to the formation of pores in the cell membrane which cause a sudden change of its conductivity [62, 63].

Electroporation is also prevented by choosing sufficiently low stimulation parameters making sure that the electric fields generated do not exceed a certain safety threshold. Nevertheless, the threshold voltages for electroporation are superior to 100V for high frequencies which makes electrochemical damage more relevant [64].

ELECTROCHEMICAL DAMAGE

During stimulation, it has to be assured that no harmful electrochemical reactions are triggered as this could potentially damage both the tissue and the electrode [2].

In order to keep the operation within safe electrochemical boundaries, two main measures are usually taken. Firstly the stimulation parameters are set within the reversible charge injection limits [65]. Additionally, the charge accumulation over multiple stimulation cycles on the tissue-electrode interface is avoided by means of biphasic stimulation and charge balancing techniques [66].

3.1.2. LONG-TERM CONSIDERATIONS

For chronic stimulation, it is crucial to study the long-term effects of electrical stimulation. Mechanical effects are predominant over electrical effects leading to connective tissue formation and neural loss. Hyper-activation and electroporation become more relevant in the long-term. The least dominant damage mechanism in the long term is electrochemical damage provided that the irreversible charge transfer mechanisms operate under the charge injection limits[67].

Given the stated dominance of mechanical effects over electrical effects and the fact that the application only requires acute stimulation, long-term effects will not be considered in the scope of this thesis.

3.1.3. GENERAL CONSIDERATIONS

As a general rule of thumb two metrics are used to asses the safety of a given electrical stimulation scheme linking two key metrics: the charge per phase, which is proportional to the total volume within which neurons can be excited, and the charge density which determines the proportion of excited neurons. The maximum safe level is given by the Shannon expression [68]:

$$log\left(\frac{Q}{A}\right) = k - log(Q) \tag{3.1}$$

Where Q is the charge per phase, Q/A is the charge density per phase and k is an experimental parameter to fit the data. This equation draws a clear boundary between the safe and unsafe electrical stimulation area.

3.2. ELECTRODE-TISSUE INTERFACE: WHEN A METAL MEETS THE TISSUE

When a metal electrode is placed inside a body tissue, an interface is formed. Metals conduct electrons and biological tissues conduct ions (sodium, potassium, chloride ...), the electrode-tissue interface (ETI) mediates the charge transfer between the two [57]. The electrode-tissue interface is a crucial issue when it comes to ensuring safety, efficiency, and reliability of electrical stimulators. The charge transfer mechanisms in the ETI can be divided into two main groups. On the one hand, in non-faradaic reactions, no electrons are transferred between the electrode and electrolyte, They only rely on redistribution of charged chemical species in the electrolyte. This capacitive coupling is usually modeled by means of a double layer capacitance (C_{dl}). On the other hand, when electrons are transferred between the electrode and the electrolyte, leading to electrochemical reactions we talk about faradaic reactions. These reactions are modeled by means of the Faradaic impedance (Z_f) which is usually approximated using a charge transfer resistor (R_{ct})[60]. Given the fact that no transfer of electrons takes place during non-faradaic reactions, they are always reversible. Faradaic reactions, on the other hand, can be non-reversible leading to damage to both the tissue and the electrode. In order to devise safe stimulation protocols, a good understanding of these processes is needed.

Faradaic reactions include a wide variety of electrochemical reactions and can be divided into cathodic processes (electrodes flow from the electrode into the electrolyte) and anodic processes (electrodes flow from the electrolyte into the electrode). Some examples of cathodic reactions include reduction of water, metal deposition, and oxide formation while oxidation of water and electrode corrosion are associated with anodic reactions. Despite the electrode transfer, some of these reactions can be reverted depending on their nature assuming that the reaction products have not dissipated into the tissue. Therefore, Faradaic reactions are usually further divided into reversible and irreversible reactions [69]. The relative rates of kinetics and mass transport are used to assess the reversibility of a given faradaic reaction. In a faradaic reaction with fast electron transfer kinetics, the chemical reaction product is not able to diffuse away from the electrode surface and it can be reversed back into its reactant form. In slow kinetics, reactions products are formed and diffused into the tissue before they can be reversed. These irreversible products include solubles, precipitates, and gases. The Warburg Impedance (Z_W) accounts for mass transfer (diffusion) limitations in these reactions and thus allows for assessment of the non-reversible charge injection [70]. The objective of safe electrical stimulation is to avoid these irreversible Faradaic reactions[60].

3.3. CHOOSING A SUITABLE ETI MODEL

Several models have been proposed throughout the years to model the Electrode-Tissue Interface. The standard ETI model, the Timmer equivalent circuit, is portrayed in Figure

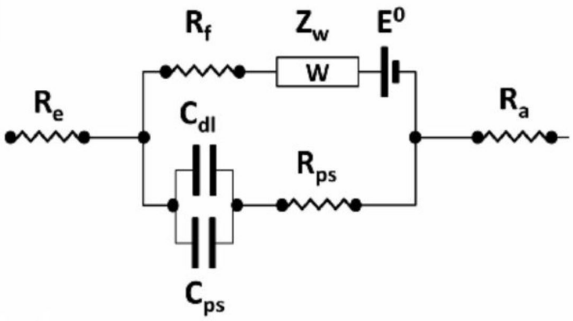

Figure 3.1: Timmer equivalent circuit representing the electrode, the ETI and the tissue [57].

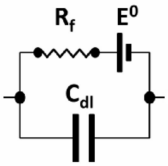

Figure 3.2: Three-element Randles equivalent circuit representing the ETI [57].

3.1. The electrode and connecting wires are modeled by the ohmic resistance R_E.[57]. Indirect charge transfer is modeled with a double-layer capacitor (C_{dl}), responsible for modeling charge redistribution and a charge transfer resistance (R_{ps}) in series with a pseudocapacitor (C_{ps}). On the other hand, direct charge transfer is composed of a Faradaic resistance (R_f) which models the direct transfer of electrons and a Warburg element (Z_w) that accounts for diffusion limitation. The battery E_0 represents the voltage at equilibrium [57].

The complex electrochemical phenomena involved in the ETI require element models that present fractional and non-linear behavior without a direct and easy implementation in standard circuit simulators. An example of such non-linearities is the asymmetry observed in the ETI voltage when an interpulse delay is present in the signal. Such behavior can only be modeled using fractional order differential equations. For this reason, circuit designers tend to linearise and simplify the models around their operating conditions. One of these simplifications is removing the negligible resistance of the electrode R_E. Furthermore, adsorption (C_{ps},R_{ps}) and diffusion limitations (Z_w) are usually neglected. A further simplification is made by replacing the constant phase capacitor C_{dl} with a simple capacitor. These simplifications lead to the commonly used three-element Randles equivalent circuit which can be appreciated in Figure 3.2. While these simplifications might be helpful for some applications they oversimplify the model and make it impossible to assess the non-reversible charge transfer mechanisms since crucial mechanisms such as ion adsorption and ion limitation are neglected. Additionally, given the wide range of frequencies, amplitudes, and waveforms to be explored, in this study, a linearization around a single operating point is not enough. In order to accurately simulate any stimulation scheme, more complex models including the non-linear

and fractal behavior of the ETI are needed.

Several experimental studies have been conducted with the intention of parametrizing the Timmer equivalent circuit accounting for its complex and non-linear properties. The standard procedure consists of applying impedance spectroscopy to the implanted electrodes and infer the parameters from the measurements. Most of the successful efforts in parametrizing the ETI have taken place in deep brain stimulation (DBS) applications using microelectrode arrays [71] given their prominent interest and research funding. Nevertheless, the difference between nerve tissue and fat and muscle tissue and most importantly the considerable differences in sizes, geometries, and properties between microelectrode arrays and normal electrodes, make it hard to extrapolate to peripheral nerve stimulation (PNS) applications. The most relevant attempts of experimental ETI characterization in peripheral nerve stimulation have been led by Kolbl et al. [72] and Sawan et al. [73].

Kölbl et al. [72] propose a multi-model approach as an alternatively to the Timmer equivalent circuit. The non-linear behavior of the system is modeled by means of multiple local linear models that are weighted by an activation function close to the operating point. Each local model is represented by the fractional transfer function:

$$Z_k(s) = K_k\left(\frac{(\frac{s}{\omega_{bk}})^{\gamma_k}+1}{(\frac{s}{\omega_{bk}})^{\gamma_k}}\right) \tag{3.2}$$

Where K_k, ω_{bk} and γ_k are fit to the experimental data of the specific local area by means of an optimization algorithm that reduces the quadratic error with the simulated time response. The validation of the model was conducted by stimulating the tissue with an arbitrary Gaussian function and comparing the normalized root-mean-square error between the measured voltage and the simulated one. This approach outperformed the linearized RC model. The main inconvenience of this particular model when it comes to applying it to the application at hand is that, while it can properly assess the ETI voltage, it is unable to provide any insight in the faradaic and non-faradaic injection currents which is a relevant metric to asses the electrochemical damage.

Sawan et al. [73] on the other hand characterize each parameter of the Timmer equivalent circuit. The proposed model is presented in Figure 3.3 and includes a constant-phase-angle impedance (Z_{cpa}), a charge transfer resistance (R_{CT}) and a Warburg impedance. The tissue is modeled by the electrolyte resistance (R_{el}). Additionally, E_{AC} accounts for the fact that the two electrodes used are in practice not identical and it is in the order of a few millivolts. The model assumes the electrode resistance and capacitance to be negligible.

The contact area is not homogeneous which is why instead of using a simple capacitor a double layer capacitance C_{dl} is used, which can be modelled as follows:

$$Z_{CPA} = \frac{1}{(j\omega C_{dl})^{\beta}}, 0 \leq \beta \geq 1 \tag{3.3}$$

where β is an empirical constant that accounts for the deviation from a normal capacitor and has a value of around 0.95. C_{dl} depends on three main factors: the permittivity, 3D overlap area and thickness of the interface. Figure 3.4(a) shows the fre-

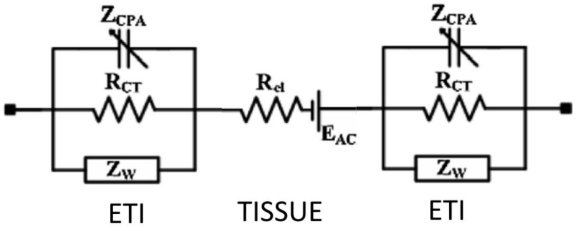

Figure 3.3: Model used by Sawan et al. [73]. The ETI model consists of a constant-phase-angle impedance (Z_{cpa}), a charge transfer resistance (R_{CT}) and a Warburg impedance. The tissue is modeled by the electrolyte resistance (R_{el})

quency response of the constant phase element impedance for values of $\beta = 0.95, \beta = 0.8$, $C_{dl} = 800nF$ and $C_{dl} = 400nF$.

The charge-transfer resistance, on the other hand, models the direct charge transfer by means of oxidation-reduction reactions and it is given by the following expression:

$$R_{CT} = \frac{RT}{nFJ_0} \tag{3.4}$$

Where R is the gas constant, α the transfer coefficient, F the Faraday constant, n is the number of electrons per molecule oxidized or reduced and J_0 is the current density under linear conditions.

Finally the Warburg impedance is in charge of modelling the diffusion of ionic species at the interface. This impedance is given by:

$$Z_w = \frac{\sigma}{\sqrt{\omega}}(1-j) \tag{3.5}$$

The Warburg coefficient σ depends on the effective contact area, diffusion coefficients and the concentration of the ions produced by the oxide-reduction reactions. Figure 3.4(b) shows the frequency response of the warburg impedance for values of $\sigma = 100k\Omega s^{-1/2}$, $\sigma = 50k\Omega s^{-1/2}$ and $\sigma = 10k\Omega s^{-1/2}$

It is important to note that, the model includes fractal order components (Z_{CPA} and Z_w) and it is non-linear given that the parameters of its components depend on the stimulation current. These two properties make it hard to simulate using conventional circuit simulators.

The model presented by Sawan et al. [73] was experimentally parametrized for cuff electrodes consisting of two equal platinum contacts of 4 mm^2 area spaced by 5 mm. It was implanted around the sacral nerve S2 which, at a more distal location, branches into the pudendal nerve. A frequency range between 1Hz and 100kHz and an amplitude sweep of $10\mu A$ to 2 mA was used in the characterization. Both in vitro and in vivo tests on dog specimens were conducted. Figure 3.5 shows an example impedance spectroscopy measurement for a stimulation amplitude of $500\mu A$. From these measurements, each parameter in the model presented in Figure 3.3 was determined. As frequencies increase the impedance converges to the resistance of the nerve R_{el}. Since the charge transfer resistance R_{CT} dominates in the low-frequency range, cyclic voltammetry at low frequency

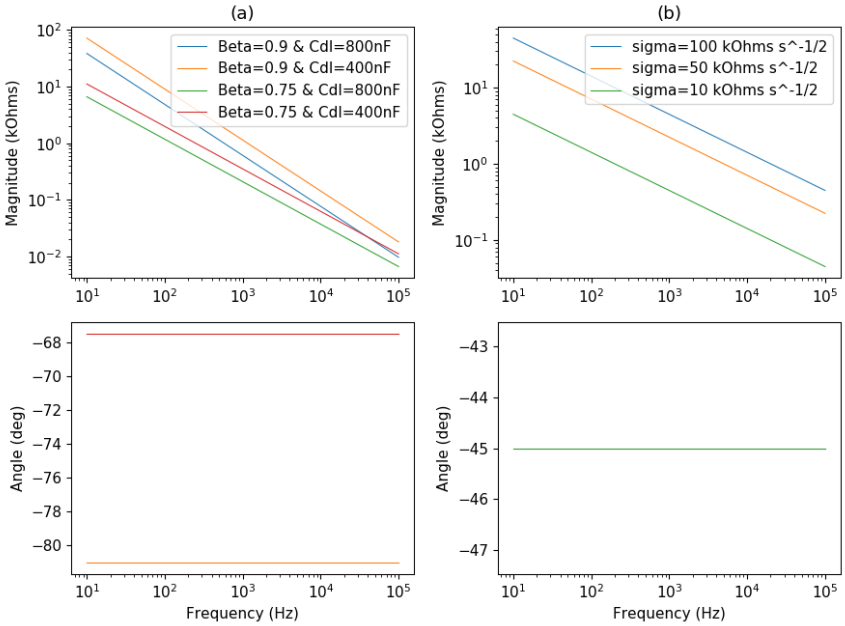

Figure 3.4: Frequency dependency of the double layer capacitance Z_{CPA} (a) and Warburg impedance Z_W (b) for different parameter values

can be used to determine its value. The rest of the parameters C_{dl},β and σ are estimated by optimization methods to fit the experimental data. Figure 3.6 shows the simulated ETI impedance for 1mA stimulation. The parameters used for the model are available in the original publication by Sawan et al. [73].

3.4. INFLUENCE OF STIMULATION PARAMETERS ON THE ETI VOLTAGE

The water window is a range of ETI potentials limited by the reduction of water leading to hydrogen gas formation at the negative end and the oxidation of water which leads to oxygen formation at the positive end. If either of these limits is reached all further charge injection is accommodated by reduction or oxidation of water, two irreversible processes that lead to damage in the tissue and the electrode [60]. For a platinum electrode within living tissue the water window has been reported to be between -0.6V and +0.9V [74]. Nevertheless, water is not the only component in the body and other ions start reacting well before reaching the limits of the water window leading to potentially damaging reaction products. Several studies have characterized these limitations using platinum electrodes in both PBS and Aplysia (a more complex ionic and physiologically plausible environment) and concluded that a narrower potential window between -0.25 to +0.55 V should be used [75]. It was also concluded that the point furthest away from both limits (0.15V) should be targeted as the steady state for safe stimulation.

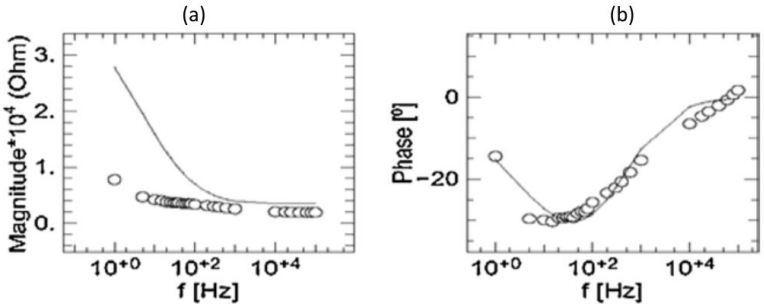

Figure 3.5: Reported impedance measurement by Sawan et al. [73] for a stimulation amplitude of 500 muA. (a) Magnitude plot(b) Phase plot

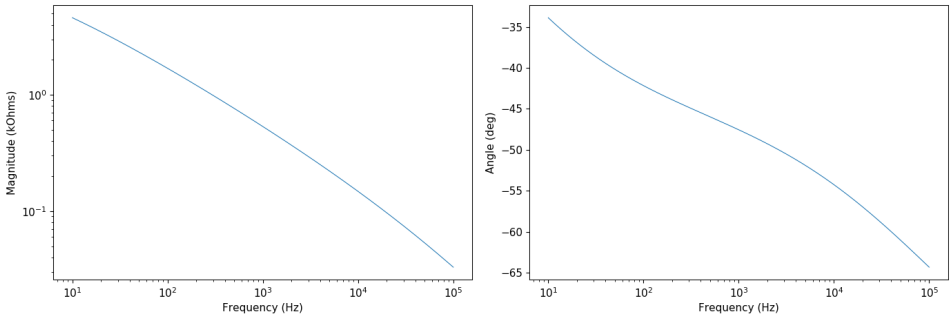

Figure 3.6: Simulated ETI impedance for 1mA stimulation. The parameters are extracted from the experimentally parametrized model presented by Sawan et al. 2007 [73]

For monophasic stimulation, each pulse moves the ETI voltage towards more negative values until all charge is injected through irreversible reactions. This sort of stimulation is only used in a few applications these days and it is not applicable to high-frequency stimulation since this irreversible injection of charge would be damaging [60].

In order to limit the irreversible processes induced by monophasic stimulation, biphasic charge-balanced schemes are used. A positive pulse following the initial negative pulse balances the charge injection to reduce the impact of irreversible reactions. In this type of stimulation, the ETI voltage drifts towards positive voltages until the charge injected irreversibly during the anodic and cathodic pulses is the same [60]. The main issue with charge balanced waveforms is that while they prevent excessive irreversible charge injection on the cathodic pulse they are likely to reach the positive safe ETI window threshold leading to anodic corrosion[60].

Biphasic charge imbalanced schemes, on the other hand, yield a lower maximum positive potential than the one achieved with charge-balanced stimulation. Having a lower maximum voltage ensures that the charge delivered into anodic Faradaic processes that lead to electrode corrosion is reduced. Charge-imbalanced biphasic waveforms provide a method to reduce unrecoverable charge in the cathodic direction and in the anodic direction. They are, therefore, an attractive scheme to minimize electrochemical damage to the tissue or the metal electrode [60].

In order to gain an intuitive knowledge of the influence of different waveform parameters on the electrochemical safety of stimulation, we run some simulations on the ETI model presented by Sawan et al. [73]. Figure 3.7 shows the evolution of the ETI voltage as different waveform parameters are altered. Analyzing these simulations one might intuitively argue that the highest frequency and smallest current might be the best solution to guarantee a safe stimulation. Nevertheless, as presented by Zhao et al. [55] the block threshold, defined as the minimum amplitude needed to achieve a successful block at a given frequency, increases monotonically with frequency for a charge balanced biphasic waveform. Figure 3.8 (a) shows the reported block thresholds. Figure 3.8(b) shows the simulated maximum and minimum ETI voltages. The increased block threshold needed at higher frequencies, contrary to the initial assumption, leads to an increase in ETI voltage window and a potentially dangerous stimulation. We see that lower frequencies, given the lower block threshold associated with them might be electrochemically safer. Additionally, Figures 3.8 (c) and (e) present the findings by Zhao et al. [55] with regard to charge imbalance . From these results, we can conclude that charge imbalance can lead to smaller threshold amplitudes which imply a higher power efficiency and an increased safety. Nevertheless, excessive charge imbalance can potentially drive the ETI voltage window to dangerous levels. These findings suggest that experimenting with different waveforms, charge balancing schemes, frequencies and amplitudes has the potential of finding a safer efficacious block.

3.5. CONCLUSION

In this chapter, important safety considerations regarding high-frequency electrical stimulation were covered. Given the acute nature of the pudendal nerve stimulation used in the treatment of urinary retention, long-term considerations are disregarded as secondary. Short-term safety is ensured by selecting sufficiently low amplitude values to

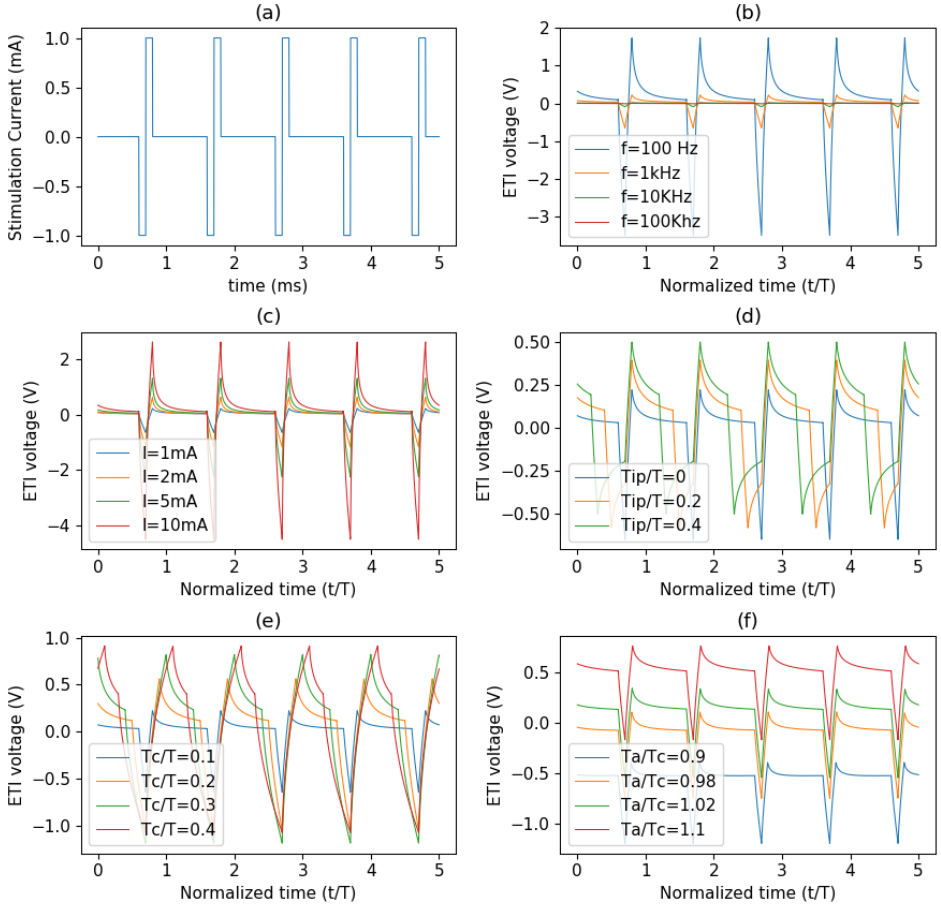

Figure 3.7: ETI voltage response to biphasic current stimulation. (a) Standard biphasic waveform $f = 1kHz, I = 1mA$,interpulse delay $T_{ip} = 0$, cathodic pulse $T_c = 0.1 \cdot T$ and anodic pulse $T_a = T_c$. In order to assess the dependency of the voltage waveform on each of the stimulation parameters, they are swept independently while the rest remain at their default values. (b) As frequency increases the voltage window decreases. (c) As current increases the voltage window increases (d) Increasing the interpulse delay allows the ETI to discharge for a longer time which effectively adds a positive offset (e) Increasing the anodic and cathodic pulse duration leads to a higher charge injection which translates into a wider voltage window. (f) Introducing a small mismatch between the two pulses causes a charge imbalance that leads to a dc offset in the ETI voltage. A larger anodic pulse leads to a positive offset while a larger cathodic pulse will cause a negative offset.

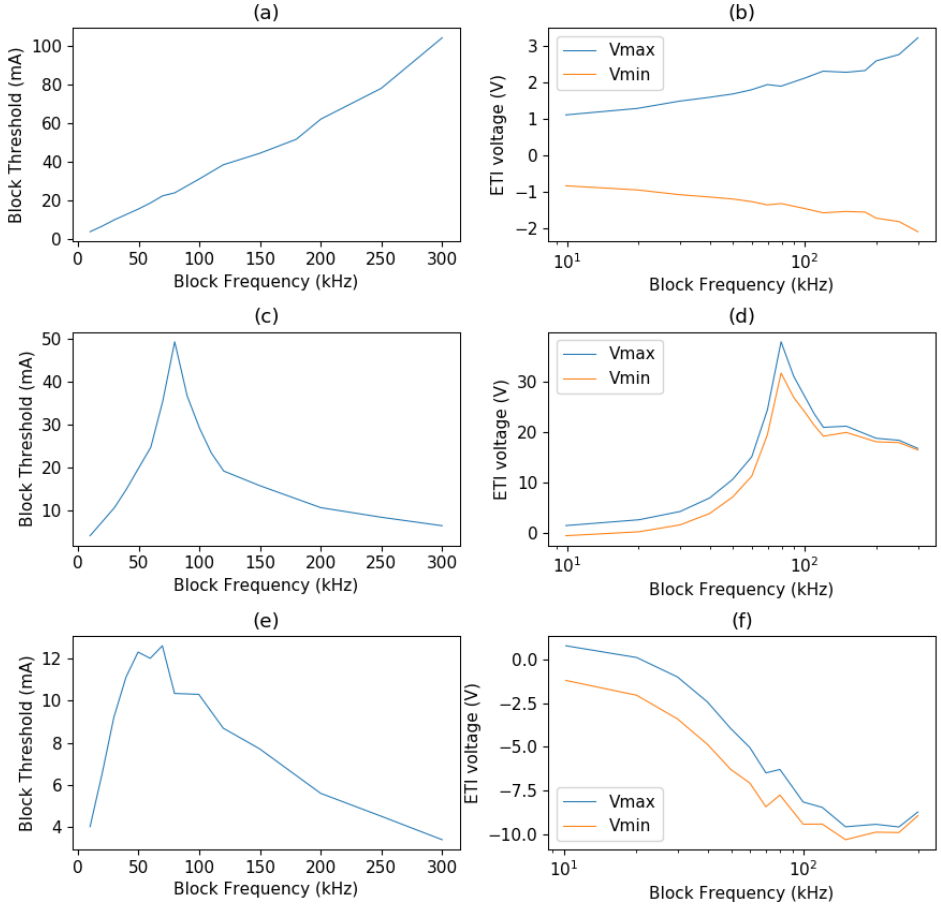

Figure 3.8: Simulated ETI voltage window for the block waveforms presented in Zhao et al. [55] Fig. 3. (a) Zhao et al. [55] Fig. 3. A For a symmetric waveform the block threshold monotonically increases with frequency. (b)Despite higher frequencies being associated with lower ETI window voltages the increased threshold current leads to an effective increase of the ETI window. (c)Zhao et al. [55] Fig. 3.B A charge imbalance making the anodic pulse $1\mu s$ longer makes the block threshold peak at 80 kHz and decrease as frequency increases. (d) The anodic imbalance brings the ETI voltage to damaging levels in spite of the decreased block threshold for high frequencies (e)Zhao et al. [55] Fig. 3.C A charge imbalance making the cathodic pulse $1\mu s$ longer makes the block threshold peak at 70 kHz and decrease as frequency increases. In this case, the block thresholds are considerably reduced (f) The cathodic imbalance brings the ETI voltage to damaging levels in spite of the decreased block threshold for high frequencies

prevent electroporation and ensuring that the ETI voltage is kept within the safe ETI window ($-0.25V < V_{ETI} < 0.55V$). This will ensure that the charge injected though irreversible non-faradaic processes is reduced to a minimum. Additionally, neural hyperactivity may cause a potentially harmful depletion of local chemical species. The assessment and modeling of neural hyperactivity need more research and falls out of the scope of this thesis.

In order to determine electrochemical safety, the use of experimentally parametrized electrode-tissue interface models is required. We propose the use of the experimentally validated ETI model presented by Sawan et al. [73] which includes the non-linear and fractal aspect of the ETI. This complex model allows for a much clearer insight into both the ETI voltage and the charge injection processes.

We have also studied the influence of each of the waveform parameters on both the ETI voltage window and the charge injection by means of faradaic reaction processes. In general terms, a higher frequency means safer stimulation as lower ETI voltage window values are achieved. Increasing the current, on the other hand, yields less safe stimulation. Additionally, small charge imbalances of around 1% can potentially lead to safer stimulation as the small offset introduced can set the ETI voltage in the center of the non-symmetrical limits of the safe ETI window.

Running the ETI model on the block thresholds reported by Zhao et al. [55] we see that the increased thresholds associated with higher frequencies make the voltages generated at the ETI increase to potentially dangerous levels. Contrary to the initial intuition, when the condition of achieving a successful block needs to be met, higher frequencies might not necessarily lead to safer stimulation. This realization motivates the need for an optimization algorithm to find the optimal stimulation parameters and waveform shape.

The ETI model presented in this chapter will be used throughout this thesis in combination with an axonal model and a differential evolution algorithm to find the optimal stimulation parameters to ensure electrochemically safe stimulation.

4

MODELLING HIGH-FREQUENCY NERVE CONDUCTION BLOCK

In order to assess the efficacy of the conduction block, a computational model able to simulate the axon response to an external stimulation waveform is needed.

In this chapter, we will analyze the different computational axonal models available with the intention of selecting the most suitable one for high-frequency conduction block. The most commonly used computational models are exposed and compared in the first section. The selected model, proposed by McIntyre, Richardson, and Grill (MRG), is then discussed in more detail. The implementation of such a model in Python and NEURON is briefly touched upon. Finally, a conclusion is presented.

4.1. COMPUTATIONAL AXONAL MODELS FOR HIGH-FREQUENCY CONDUCTION BLOCK

In-vivo clinical research is crucial to the understanding of nerve electrophysiology. Nevertheless, clinical tests are slow, expensive, require specialized staff and equipment and involve ethical concerns. With the intention of circumventing all these issues, several electrophysiological computational models of nerves are commonly used as preliminary studies that manage to reduce the number of clinical tests needed [76].

Throughout the years, several axon models have been proposed. The first mathematical model, proposed by Hodkin and Huxley model (HH)[31], was based on experimental measurements performed on a squid. In spite of the HH model being proposed in 1952, it is still used in state-of-the-art research today. In 1964, Frankenhaeuser and Huxley (FH) [32] proposed an alternative model using measurements on frog specimens. Chiu et al. [33] proposed in 1979 the CRRSS model using experimental rat data. In 1995 the SRB model was introduced [34] using experimental rabbit data. Finally, McIntyre et al. 2002 [35] proposed a mammalian axonal model, MRG, based on experimental human, cat and rat data.

It is important to note that each of these models has only been validated in a specific frequency range. This makes clinical tests strongly advised to validate the findings obtained using these computational models [50].

Several studies have used the HH and FH models [55, 77]. Nevertheless, the MRG model provides a more reliable response for higher frequencies which explains why it is the golden standard today [12, 45, 53]. The MRG model has been extensively validated against published experimental data not only in action potential elicitation [78] but also in high-frequency stimulation [51, 79].

4.2. OVERVIEW OF THE MRG MODEL

The MRG model is a double cable mammalian nerve fiber model which includes representation of the nodes of Ranvier and the paranodal and internode sections. Additionally, the impedance of the myelin sheath is finite, as opposed to other models [35].

The structure representation of the model, as well as its equivalent lumped circuit membrane model can be appreciated in Figure 4.1(a). The membrane dynamics at the node are modeled by a membrane capacitance (C_n) in parallel with a linear leakage conductance (Lk) and three non-linear ionic conductances (a slow potassium conductance (Ks), a fast sodium conductance (Naf) and a persistent sodium conductance (Nap)). The dynamics in the internode segments are represented by a double cable structure which includes the myelin sheath conductance (G_m and C_m) and the axon membrane (G_i and C_i). Finally, the paranodal compartments introduce the conductances G_p and G_a. Figure 4.1(b) shows the electrical parameters of the model. Figure 4.1(c) shows the experimentally obtained geometric dimensions of each section on the model depending on the diameter of the fiber. All equations describing the dynamics of the model are available in its original publication [35]

Figure 4.2(a) shows the setup used for simulations of high frequency conduction block. The standard setup used in simulation studies consists in eliciting an action potential at one end of an axon which will propagate to the other end. The blocking electrode is placed at the desired location along the axon. The successfulness of the block is assessed by measuring the activity at the opposite end of the axon.

One of the requirements is to ensure a complete block of the pudendal nerve. Previous studies have extensively demonstrated that smaller axon diameters need a higher amplitude to achieve a successful block [80]. Therefore this study will focus on an axon diameter of $5.7\mu m$, the smallest axon diameter available in the MRG model, which is comparable to the smallest fibers in the pudendal nerve with an approximated diameter of $5\mu m$ [26, 27]. This will ensure a safe block of all larger diameters.

An MRG axon model with a total of 50 nodes is used in the simulations. For the chosen diameter of $5.7\mu m$ this leads to an axon length of $25mm$.

An external electrode used for the high-frequency block is placed as a point source in an infinite homogeneous medium with a resistivity of $500\Omega - cm$ as used by similar peripheral nerve simulation studies [80]. The electrode is placed right on top of node number 25 at a distance of 1.6 mm, which corresponds to the maximum radius of the pudendal nerve cross-section. The high-frequency stimulation starts at $t = 0$. At $t = 15ms$ an action potential is generated at node 0 that will propagate down to node 50. The membrane activity at node 50 is monitored to assess the efficacy of the conduction

(a)

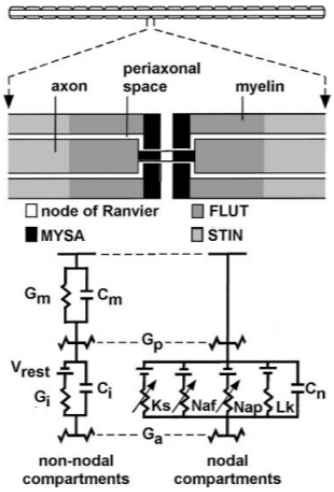

(b)

Nodal capacitance[a] (c_n)	2 μF/cm^2
Internodal capacitance[b] (c_i)	2 μF/cm^2
Myelin capacitance[c,d,e] (c_m)	0.1 μF/cm^2
Axoplasmic resistivity (ρ_a)	70 Ω cm
Periaxonal resistivity (ρ_p)	70 Ω cm
Myelin conductance[c,d,e] (g_m)	0.001 S/cm^2
MYSA conductance (g_a)	0.001 S/cm^2
FLUT conductance (g_f)	0.0001 S/cm^2
STIN conductance (g_i)	0.0001 S/cm^2
Maximum fast Na^+ conductance[f,g,h] (g_{Naf})	3.0 S/cm^2
Maximum slow K^+ conductance[f,h,i] (g_{Ks})	0.08 S/cm^2
Maximum persistent Na^+ conductance[j] (g_{Nap})	0.01 S/cm^2
Nodal leakage conductance (g_{Lk})	0.007 S/cm^2
Na^+ Nernst potential[k] (E_{Na})	50.0 mV
K^+ Nernst potential[k] (E_K)	−90.0 mV
Leakage reversal potential (E_{Lk})	−90.0 mV
Rest potential[k] (V_{rest})	−80.0 mV

(c)

	Fiber Diameter								
	5.7	7.3	8.7	10.0	11.5	12.8	14.0	15.0	16.0
Node-node separation	500	750	1,000	1,150	1,250	1,350	1,400	1,450	1,500
Number of myelin lemella	80	100	110	120	130	135	140	145	150
Node length	1	1	1	1	1	1	1	1	1
Node diameter	1.9	2.4	2.8	3.3	3.7	4.2	4.7	5.0	5.5
MYSA length	3	3	3	3	3	3	3	3	3
MYSA diameter	1.9	2.4	2.8	3.3	3.7	4.2	4.7	5.0	5.5
MYSA periaxonal space width	0.002	0.002	0.002	0.002	0.002	0.002	0.002	0.002	0.002
FLUT length	35	38	40	46	50	54	56	58	60
FLUT diameter	3.4	4.6	5.8	6.9	8.1	9.2	10.4	11.5	12.7
FLUT periaxonal space width	0.004	0.004	0.004	0.004	0.004	0.004	0.004	0.004	0.004
STIN length	70.5	111.2	152.2	175.2	190.5	205.8	213.5	221.2	228.8
STIN diameter	3.4	4.6	5.8	6.9	8.1	9.2	10.4	11.5	12.7
STIN periaxonal space width	0.004	0.004	0.004	0.004	0.004	0.004	0.004	0.004	0.004

Values are expressed in μm.

Figure 4.1: MRG model definition [35] (a) Membrane model (b) Electrical Parameters (c) Geometrical parameters

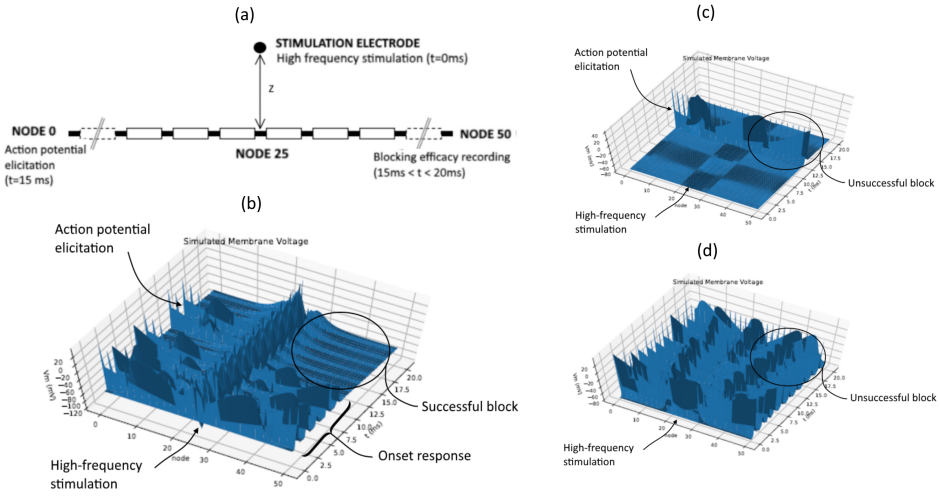

Figure 4.2: MRG model simulation setup and example results (a) Simulation Setup. An extracellular electrode is placed at a distance Z of node 25. High frequency stimulation starts at $t = 0$. An action potential is elicited at node 0 at $t = 15ms$. The action potential is quickly propagated down the axon. In a successful conduction block, the propagation of the action potential is interrupted at node 25 and never reaches node 50. In an unsuccessful block, the action potential manages to propagate past node 25. The presence of an action potential at node 50 between $t = 15ms$ and $t = 20ms$ is used to assess the effectiveness of the conduction block. (b) Example of a successful conduction block (20 kHz, 0.2mA, sine-wave). The 3D mesh plot shows the membrane potential depending on node location and time. The high-frequency stimulation at node 25 from $t = 0$ leads to a high membrane activity. During the first 10 ms after activation of the high-frequency signal, a set of action potentials generated. This phenomenon is referred to as the onset response and has been reported to always take place [9]. At $t = 15ms$ a test action potential is elicited in node 0. The conduction of the test action potential is interrupted at node 25. (c) Example of an unsuccessful conduction block. (20 kHz, 0.2mA, sine-wave). The low amplitude used fails to achieve a conduction block and the test action potential is propagated through the whole axon. (c) Example of an unsuccessful conduction block (0.5 kHz, 2mA, sine-wave). The low frequency used leads to an elicitation of several action potentials. This phenomenon is usually referred to as repetitive firing

block. A successful conduction block takes place when no action potential is measured at node 50 from $t = 15ms$ to the end of the simulation. The runtime of the simulation is 20 ms using a standard timestep of $dt = 1\mu s$.

Figure 4.2 (b) shows the results of a simulation leading to successful conduction block while Figures 4.2 (c) and (d) show to possible examples of an unsuccessful block.

4.3. MRG MODEL IMPLEMENTATION

Initially, the MATLAB implementation of the MRG model used by Danner et al. and Krouchev et al. [81, 82] was used. The computational expenses associated with such model proved too high of a burden which motivated the use of the original NEURON implementation of the MRG model as proposed by McIntyre et al.[35]. This version was adapted to include an extracellular electrode for high-frequency stimulation placed in an infinite homogeneous medium. A Python script was used as an interface between

the NEURON environment and the optimization algorithm.

5

DEVISING ALGORITHMS FOR HIGH-FREQUENCY BLOCK WAVEFORM OPTIMIZATION

Classical analytical optimization approaches require the function under test to be linear, continuous and differentiable. Both the ETI model and the axonal neural model used are highly non-linear, rendering most analytical approaches not applicable. Additionally, given the high dimensionality of the search space and the high computational expenses involved in the simulation of the models, sweeping through all different points in the search space is not possible [12]. These type of problems are well suited for stochastic swarm intelligence optimization algorithms.

In this chapter, an overview of the main stochastic swarm intelligence optimization algorithms is given to justify the selection of the most appropriate one for our application. Later, several aspects of the chosen optimization algorithm are fine-tuned for maximal performance. Special attention is put in the description of the innovations added by this work. These aspects include the fitness function, the waveform representation scheme, the optimization parameters as well as substantial modifications to the standard algorithm. In a later section, the software implementation of the algorithm and hardware resources used for its execution are briefly covered. Finally, a conclusion summarizing the main findings and contributions of the chapter is given.

5.1. SELECTING THE APPROPRIATE STOCHASTIC SWARM INTELLIGENCE ALGORITHM

Stochastic swarm intelligence algorithms have attracted a lot of attention given their efficient optimization of computationally expensive, non-linear and discontinuous functions. The main two characteristics that embody all stochastic swarm intelligence algorithms are self-organization and division of labor. Self-organization relies on positive

and negative feedback which help in amplification and stabilization of the system, random fluctuations that ensure an adequate exploration of the search space and swarm interactions where information is shared among the individuals. The second property, division of labor, consists of the presence of multiple individuals that explore a different part of the search space and communicate to work together to find the global maxima of the problem. Additionally, this division of labor makes Stochastic Swarm Intelligence algorithms highly parallelizable which can be a crucial attribute in computationally expensive optimization problems [83]. Wahab et al. [83] reviewed seven Swarm Optimization Algorithms (GA, ACO, DE, PSO, ABC, GSO, and CSA) and concluded that Differential Evolution outperformed the rest of the algorithms in 24 of the 30 optimization problems used as a benchmark. DE was closely followed by Particle Swarm Optimization (PSO) and Genetic Algorithms (GA). Similar results have been obtained in a long list of studies acknowledging a clear dominance of Differential Evolution closely followed by PSO and GA [84–87]. In this section, these three top performing algorithms will be reviewed explaining their basic operating principles and highlighting previous applications in the field of neural stimulation optimization. The goal of this review is to lead to a justified selection of the best algorithm for high-frequency block waveform optimization.

5.1.1. PARTICLE SWARM OPTIMIZATION

Particle Swarm Optimization (PSO) is inspired by the swarm behavior of fish schooling and bird flocks. Several particles are initialized randomly across the search space and the fitness at each point is evaluated. Each particle has a position and a velocity that will determine the point in space they will explore in the next time step. Throughout exploration, records of the individual and global best positions are kept and they are used to update the position and velocity of each particle in each time-step. Early in the optimization process, in order to entice exploration, the particles move to try to find a local optimum by following their own records. As time progresses the tracked best positions of neighboring individuals start gaining a much more relevant role in updating the velocity of each particle which promotes exploitation. Finally, the global maximum is used to allow all particles to exploit it.

Particle swarm optimization was used by Peña et al in their study of the optimal electrode configuration and stimulation amplitude to increase effectiveness (maximize activation in regions of interest and minimize activation in regions of avoidance) and minimize power consumption in Deep Brain Stimulation [15].

5.1.2. GENETIC ALGORITHM

The Genetic Algorithm (GA), originally proposed by John Holland in 1975 [88], is based on the mechanics of natural selection. Strong individuals are more likely to adapt, survive and pass their genetic traits to next generations than weak individuals who have a tendency to perish. If this phenomenon is analyzed at a population level, one might argue that the total fitness of the population has a tendency to increase tending towards an optimal point. Taking this principle as inspiration, the GA algorithm relies on a population of individuals with a set of genes that are representative of a potential solution to the optimization problem, in our case a stimulation waveform. Each of these individual solutions is ranked based on the fitness function that aims to be optimized. A new pop-

ulation is formed by means of selection, crossover, and mutation based on the fitness ranking.

The GA starts by generating an initial population which can be performed either randomly, usually with a limited range of the search space, or by means of a heuristic function that predicts optimal individuals in a computationally inexpensive way. Later the population is evaluated on the fitness function and a fitness value is associated with every individual.

In the selection stage, a set of individuals is passed to the next generation while the rest are dropped out. One of the simplest implementations is to select the N fittest individuals. In some applications, this approach can lead to excessive exploitation of the initial local optima. Alternative selection techniques aim at solving this issue. In roulette wheel selection the chance of selecting a specific individual is linearly proportional to its fitness value. Rank selection follows a similar approach but the chance of selection is now proportional to the position of the individual in the population's ranking. This method is usually applied when there are magnitudes of order of difference in fitness values which would reduce rank selection to the initial fittest selection. Tournament selection chooses K random individuals from a population and the best individual is chosen. The process is repeated until the new generation is formed completely.

The next stage in the GA algorithm is crossover, which exchanges and mates the genes of different individuals to find potentially fitter individuals. Traditionally, crossover was implemented in a single location but alternative methods propose multiple-point crossover or blending. Finally, the mutation step occurs by altering genes. This stochastic process allows the method to explore new areas in the search space. The evaluation and generation of new populations are repeated until an optimal solution or a termination criterion are met. One of the main drawbacks of the system is its slow convergence which can be tackled by carefully designing each of its steps to the specific problem at hand.

Genetic algorithms have been extensively used in the optimization of neural stimulation schemes. Feng et al [11] used genetic algorithms in Deep Brain Stimulation applications. Kent and Grill [13] used a genetic algorithm to find optimal nerve cuff designs for selective stimulation of the pudendal nerve. In order to increase the efficiency of brain stimulation in treating Parkinson's and reduce the energy required, Brocker et al. [14] used a genetic algorithm to find the optimal stimulation pattern. In the pursuit of an energy-optimal waveform shape for neural stimulation, Wongsarnpigoon et al. used a genetic algorithm to optimize the waveform shape [12].

5.1.3. DIFFERENTIAL EVOLUTION

Differential evolution (DE) shares many similarities with Genetic algorithms: a population of individuals is improved over several generations by means of crossover, mutation and selection operators. Similarly to GA, in DE, an initial population is generated and the fitness of each individual is evaluated. At the beginning of each generation, a process referred to as mutation takes place following the expression:

$$v_{i,G+1} = x_{r1_G} + F(x_{r2,G} - x_{r3,G}) \tag{5.1}$$

Where F is a scaling factor in the range of $[0,1]$ and the vectors $x_{r1,G}$,$x_{r2,G}$ and $x_{r3,G}$ are chosen randomly from the current generation G with the condition $r1 \neq r2 \neq r3 \neq i$.

Later, in the recombination or crossover stage, a child is generated by taking each of its genes from the mutated vector or from the parent. In this process, the crossover probability CR determines the likelihood of each gene being taken from the mutated vector as opposed to the parent. Finally, the fitness of the resulting child and its parent are compared and the fittest individual advances to the next generation.

Mezura et al. [89] proposed several changes in the standard Differential Evolution algorithm and analyzed their performance on 13 benchmark problems. Three sections of the algorithm were changed and all possible permutations were taken as alternative algorithms in the benchmarking. Their results clearly indicate that DE/best/1/bin outperformed the rest of the variants proposed regardless of the type of function to optimize [89]. This algorithm uses the best solution in the current population instead of a random one to find the search directions, uses only one pair of additional random solutions in the recombination and uses binomial recombination. Applying these changes the standard mutation expression presented in Equation 5.1 is replaced by:

$$v_{i,G+1} = x_{best_G} + F(x_{r2,G} - x_{r3,G}) \tag{5.2}$$

Where x_{best_G} corresponds to the waveform with the best fitness in the current generation.

To this date, no studies have been reported in the field of neural stimulation optimization using Differential Evolution. Given the extensively demonstrated success of DE over other alternatives such as PSO or GA, its robustness and simplicity (only 3 parameters are used) this optimization technique will be used in our study. In particular, we will use the DE/best/1/bin variation proposed by Mezura et al. [89] as it demonstrated dominance over the other alternatives. The use of this algorithm represents an innovation over the current state-of-the-art in the optimization of neural stimulation parameters which, as we have seen, focuses solely on PSO and GA.

While differential evolution has proven to consistently outperform other alternative algorithms in several comparison studies [83], it still presents considerable limitations, namely, premature convergence and long execution time. Increasing population size or reducing the problem dimensionality are easy ways of addressing these problems. An additional measure is to make the scaling factor F and crossover ratio CR adaptive with time starting at high values initially and decreasing over time. This approach effectively prioritizes exploration in early generations and exploitation in later generations. Another alternative is to introduce elitism by making sure that the top performing solutions are always kept in the population [90]. In general, careful design of the optimization algorithm while taking into account application-specific aspects promises to boost performance. In the following sections, this design process will be discussed relating the choice of parameters and several proposed improvements to the current state of the art.

5.2. THE IMPORTANCE OF THE FITNESS FUNCTION

The fitness function gives a quantitative measure of the efficiency, efficacy and electrochemical safety of a given stimulation waveform. This score is computed using relevant

simulation results and guides the optimization algorithm towards the appropriate direction. The performance of the optimization algorithm is strongly related to the fitness function. In this section, we describe the design of the fitness function and motivate its choice by comparing several alternatives.

In order to compose the fitness function, two key metrics are used. On the one hand, the successfulness of the conduction is assessed by running an MRG simulation with the waveform under test. If the test action potential generated on one side of the axon does not propagate to the other end it is considered a successful block. Alternatively, if the action potential reaches the other end of the axon a failed block is reported. This result is stored as a binary variable called $blocked$. The second metric used is the ETI voltage. In particular,its maximum $V_{ETI,max}$ and minimum $V_{ETI,min}$ values in the stationary response are measured. The goal is to minimize the absolute distance between these two points and the safe voltage V_{safe} defined as the midpoint of the safe ETI potential window reported in literature. For platinum this voltage is 0.15V [75]

In order to ensure successful block and minimize the ETI voltage one could propose the following polynomial fitness function:

$$Fitness = K_{blocked} \cdot blocked - K_{ETI} \cdot (|V_{ETI,max} - V_{safe}| + |V_{ETI,min} - V_{safe}|) \quad (5.3)$$

Where $K_{blocked}$ and K_{ETI} are two constants to be adjusted.

It has been demonstrated that adjusting the selectivity of the fitness function by using an exponential function yields improved performance and faster convergence [91]. Therefore the following alternative fitness function is proposed:

$$Fitness = K_{blocked} \cdot (blocked - 1 + e^{-K_{ETI} \cdot (|V_{ETI,max} - V_{safe}| + |V_{ETI,min} - V_{safe}|)}) \quad (5.4)$$

Figure 5.2 presents a performance comparison of three optimization algorithms using three proposed fitness functions. The results clearly show that the convergence speed when using an exponential fitness function is considerably higher. The polynomial fitness function achieved an optimal voltage window of -0.267 and +0.298 V while both the exponential fitness functions allowed the algorithm to reach an optimum of -0.12 and +0.15V in the same number of generations. The differences between the two differently parametrized exponential functions were not significant and $K_{ETI} = 1$ is chosen.

5.3. DEFINING THE SEARCH SPACE. A COMPARISON OF DIFFERENT WAVEFORM REPRESENTATION SCHEMES

In order to guarantee an optimal solution and a high enough convergence speed, it is crucial to properly define the search space the optimization algorithm will operate on. If the search space is too wide the speed of convergence will be prohibitively low. Oversimplifying and limiting the space can prevent the algorithm from finding the global optimum. It is, therefore, crucial to use application-specific information to define a suitable search-space. In our case, the search-space should properly define the waveform. In this section, multiple schemes for waveform representation are analyzed and compared.

In general terms, two main approaches can be followed. The waveform can be represented in the time domain or in the frequency domain. Nearly all the literature available

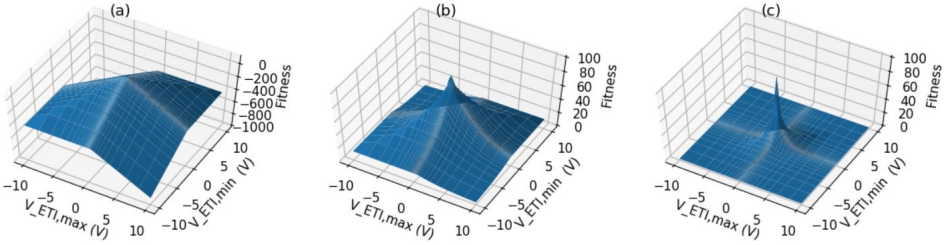

Figure 5.1: Proposed fitness functions as a function of $V_{ETI,max}$ and $V_{ETI,min}$ assuming $blocked = TRUE$. In the case of $blocked = FALSE$ all waveform graphs would be shifted by $-K_{blocked}$ (a) Polynomial fitness function presented in Equation 5.3 with $K_{blocked} = 100$ and $K_{ETI} = 50$ (b) Exponential fitness function presented in Equation 5.4 with $K_{blocked} = 100$ and $K_{ETI} = 0.2$(c) Exponential fitness function presented in Equation 5.4 with $K_{blocked} = 100$ and $K_{ETI} = 1$(

5

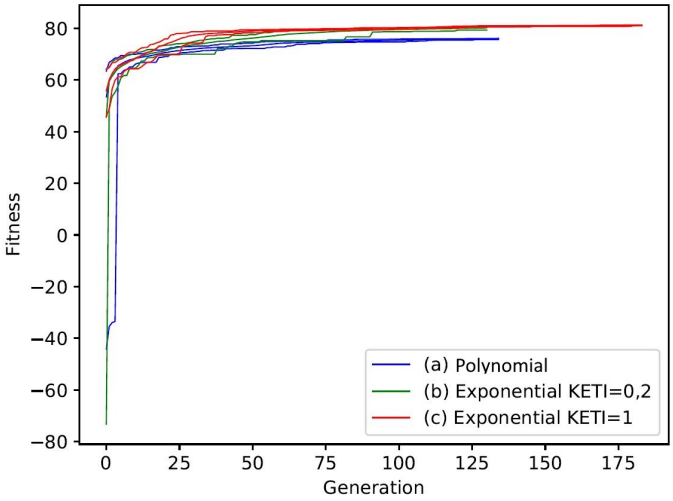

Figure 5.2: Performance of the optimization algorithm using three proposed alternative fitness functions. In order to compare the results all performances are evaluated using Equation 5.3. (a) Polynomial fitness function presented in Equation 5.3 with $K_{blocked} = 100$ and $K_{ETI} = 50$ (b) Exponential fitness function presented in Equation 5.4 with $K_{blocked} = 100$ and $K_{ETI} = 0.2$(c) Exponential fitness function presented in Equation 5.4 with $K_{blocked} = 100$ and $K_{ETI} = 1$

in the field of neural stimulation analyses waveforms in the time domain. Additionally, nearly all meaningful metrics (amplitude, frequency, inter-pulse delay ...) are defined in the time domain. Using frequency domain representation would be an impediment during validation and comparison with the available literature. Therefore, representation of the waveform in the time domain is chosen as a requirement.

One of the simplest forms of representation in the time domain consists on representing the waveform as a set of amplitudes at different discrete times with a fixed time-step. The problem with this simple approach is its lack of orthogonality. Crucial waveform parameters such as frequency and amplitude cannot be represented directly. A common improvement is to store the frequency, amplitude, and normalized waveform shape independently. Figure 5.3 (a) and (b) show the usual waveform representation scheme.

This approach still shadows relevant information such as anodic and cathodic pulses, inter-pulse delay and most importantly charge imbalance. Adding these aspects to the waveform representation could potentially lead to faster convergence of the optimization algorithm.

From literature, we know that, while slight charge imbalance might potentially lead to a safer stimulation by adding an offset to the ETI voltage and thus reducing any excessive anodic or cathodic reactions, it is important to keep a balanced charge injection to prevent irreversible damage. Limiting the search-space to charge balanced waveforms could potentially lead to a faster convergence. The proposed implementation relies on splitting the waveform period representation in a cathodic pulse and an anodic pulse. In the waveform reconstruction process, the amplitude of the anodic pulse is adjusted to make sure the same amount of charge is injected as in the cathodic pulse. As in the previous representation, frequency and amplitude are stored separately. Additionally, the ratio between cathodic and anodic periods can be adjusted. In order to asses, the influence of slight charge imbalances, a charge imbalance ratio is included in the representation. Figure 5.3 (c) and (d) present the proposed representation method. The cathodic and anodic shapes are stored separately and two new metrics, the charge imbalance, and the duty cycle are included. The charge imbalance is defined as the desired ratio of injected charge between the cathodic and anodic pulses. A charge injection of 1 ensures a perfectly balanced charge injection, smaller values result in a greater anodic charge injection while bigger values lead to greater cathodic charge injection. The duty cycle is defined as the ratio between the cathodic period and the total signal period. In the waveform reconstruction process, the waveforms are multiplied by the amplitude and the cathodic period is multiplied by -1. Then the duty cycle is used to adjust the width of each pulse. Later, the amplitude of the anodic waveform is adjusted to ensure the desired charge imbalance ratio. Finally, the waveform is repeated with the desired frequency.

An additional improvement is proposed in Figure 5.3(e) and (f) by adding two inter-pulse delays after each pulse. The reconstruction of such waveform follows the same steps as the previously described reconstruction with the addition of these interpulse delays.

Figure 5.4 shows the performance comparison of three optimization algorithms using the three proposed waveform representations. Contrary to our initial expectations

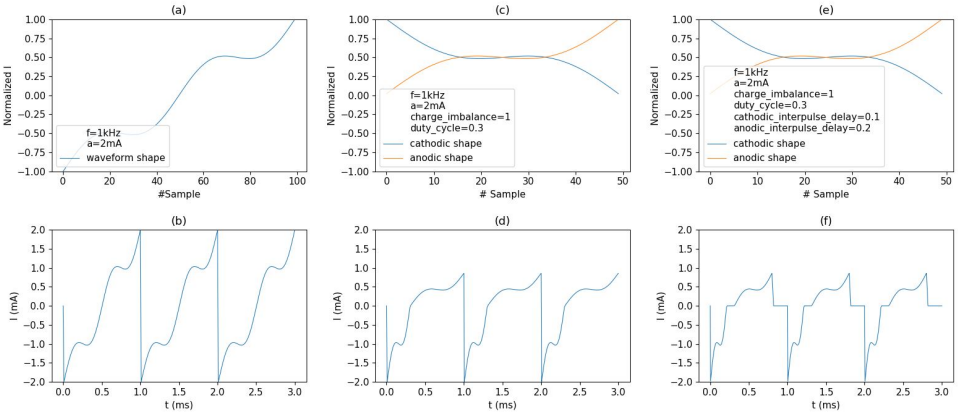

Figure 5.3: Examples of the three waveform representation schemes discussed and their reconstruction procedure (a) Arbitrary waveform representation including the signal frequency, amplitude, and waveform shape (b) Reconstruction of the signal using the arbitrary waveform representation. The normalized waveform shape is multiplied by the amplitude and repeated with the given frequency (c) Charge balanced waveform representation dividing the waveform into cathodic and anodic pulses and including charge imbalance and duty cycle. (d) Waveform reconstruction using the charge balanced waveform representation. Both cathodic and anodic pulses are multiplied by the amplitude and concatenated. The cathodic pulse is mirrored. The cathodic and anodic periods are adjusted according to the duty cycle. The amplitude of the pulse injecting the most charge is reduced until both pulses inject the same charge. The charge ratio is enforced by lowering the amplitude of the corresponding pulse. (e) Charge balance and interpulse delay waveform representation. Two inter-pulse delays are added, represented as a fraction of the total signal period. (f) Waveform reconstruction using the charge balance and interpulse delay waveform representation. The corresponding delays are added between the pulses and the periods of the pulses are reduced as needed.

the arbitrary waveform representation performed better than the two orthogonal representations proposed. Two main theories explain these results. A crucial one is the fact that unlike the other two representations, the arbitrary waveform representation allows the exploration of slightly charge imbalanced waveforms which manage to add the needed offset to get closer to $V_{safe} = 0.15V$. Additionally, the arbitrary waveform representation, as opposed to the two orthogonal improvements proposed, does not presuppose any constraints with regard to waveform shape which allows it to explore a wider search space.

5.4. OPTIMIZATION PARAMETERS

There are three main control parameters in a differential algorithm: the scale factor F, the crossover ratio CR and the population size NP. The searching capability and convergence speed show a tight relationship between these parameters, which is why it is crucial to properly tailor them to the application. In this section, we will try to grasp an understanding of how each of these parameters influences the performance of the algorithm and provide a guideline for choosing them.

Previous studies indicate that the population size should be between 3D and 8D [92]. The dimensionality of our problem, taking into account the value of each position is 108.

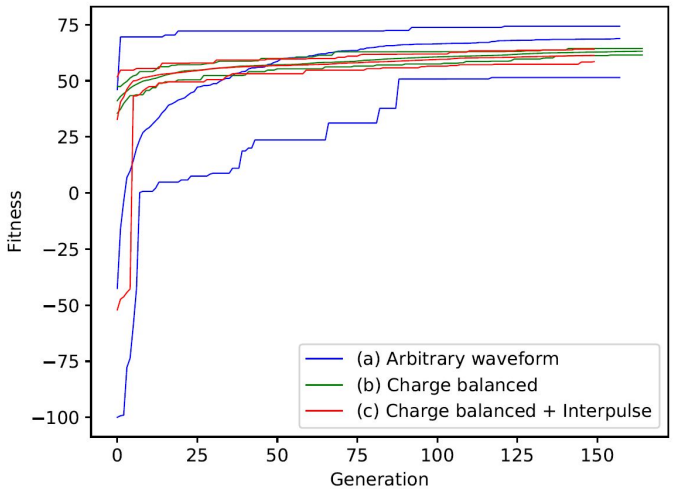

Figure 5.4: Performance of three optimization algorithms using the three alternative representation algorithms. (a) Arbitrary waveform representation (b) Charge balanced Cathodic+Anodic waveform representation. (c) Charge balanced Cathodic+Anodic and Inter-pulse Delay waveform representation.

Due to hardware limitations, only a factor of 2D can be achieved. To achieve a maximum speed-up it is advisable that the population size is a multiple of the number of processors used which is why a population of 256 is chosen.

When it comes to the scale factor F, several studies indicate it should be between 0.4 and 1 [92, 93]. We choose the widely used value of $F = 0.6$. In general terms, it is important to understand that small values of F will lead to exploitation of the current best solutions while larger values entice an exploration behavior since bigger modifications are introduced in the population [94].

The crossover ratio CR, should be between 0.3 and 0.9 [92]. If the function is separable, low values of CR are advised. Given that our function is nonseparable and their parameters are dependent on each other, higher values for CR are recommended [92]. Following this guideline, $CR = 0.8$ is chosen.

Given the importance of these parameters, several studies have proposed techniques to find their optimal values. One approach relies on having both parameters picked from a normal distribution for every individual in the population [94]. In order to evaluate this technique, we will have a mean value of 0.6 and a standard deviation of 0.3 for F and a mean value of 0.8 and a standard deviation of 0.1 for CR.

An alternative approach is to adapt these parameters based on the current performance of the system [95]. We propose adapting F and CR linearly dependent on the elapsed time. As execution time progresses the parameters linearly decrease from a starting point until an end point. The chosen values are $F_{start} = 0.9$, $F_{end} = 0.3$, $CR_{start} = 1$ and $CR_{end} = 0.6$.

Finally, another trend is to include the F and CR parameters in the genes of each individual and subject them to evolution [96]. The initial values are drawn from two normal distributions with a mean value of 0.6 and a standard deviation of 0.1 for F and

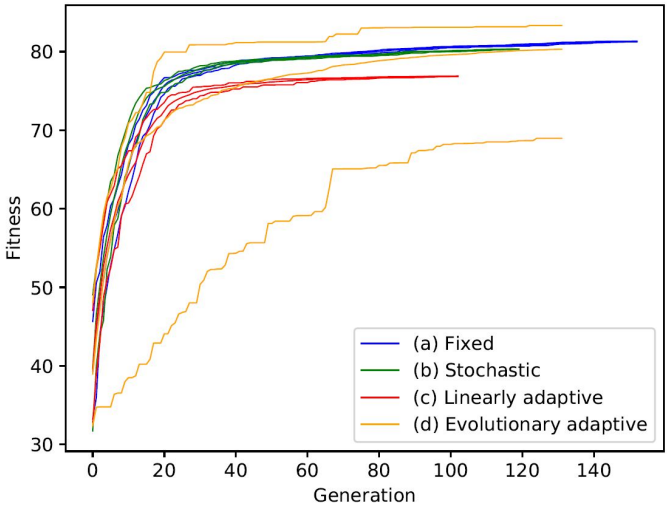

Figure 5.5: Performance of the four proposed CR and F adaptation schemes. (a) Fixed parameters ($F = 0.6$ and $CR = 0.8$). (b) Stochastic parameters. The parameters are drawn from a normal distribution ($\mu_F = 0.6, \sigma_F = 0.3$ and $\mu_{CR} = 0.8, \sigma_{CR} = 0.1$). No significant improvement with respect to fixed parameters is appreciated. (c) Linearly adaptive parameters. At the beginning of the evolution, the parameters are set to high values to prioritize exploration and they are linearly reduced until reaching a minimum at the end of evolution to prioritize exploitation ($F_{start} = 0.9$, $F_{end} = 0.3$, $CR_{start} = 1$ and $CR_{end} = 0.6$). The results show a worse performance due to early stagnation in local optima. (d) Evolutionary adaptive parameters. Initially, the parameters are drawn from a normal distribution ($\mu_F = 0.6, \sigma_F = 0.3$ and $\mu_{CR} = 0.8, \sigma_{CR} = 0.1$), they are incorporated in the genes of each individual and they are evolved by means of differential evolution along with the rest of the parameters. This method achieves the same average fitness as the fixed parameters and shows a slower convergence speed. Nevertheless, its maximum fitness is considerably greater than the rest and promises to outperform the other methods in longer runs.

a mean value of 0.8 and a standard deviation of 0.1 for CR. In each mutation step, the parameters included in the parent's genes are used.

Figure 5.5 compares the performance of different CR and F updating schemes. The population size is kept constant to 256. Using stochastic parameters drawn from a normal distribution does not provide any improvement with respect to the fixed parameters approach. The linearly adaptive approach proved a worse performance. The evolutionary adaptive scheme, where the CR and F parameters are embedded in the genes of each individual and evolved by means of differential evolution, proved the most promising scheme. The average fitness is slightly lower than that of the fixed parameters and it shows considerably lower convergence speed. Nevertheless, the maximum fitness clearly outperforms the rest. Additionally, as opposed to the rest of the presented approaches, it manages to preserve a wide variance in its population, an aspect highly needed to prevent early stagnation on local optima. For all these reasons, the evolutionary adaptive scheme will be adopted.

5.5. IMPROVED DIFFERENTIAL EVOLUTION ALGORITHM FOR HIGH-FREQUENCY BLOCK OPTIMIZATION

In this section, we present three proposed application-specific improvements to the original DE/best/1/bin algorithm and analyze their improvement on performance separately. We initially cover similar attempts of using application-specific information to improve the performance of optimization algorithms. Later we analyze in detail each of the three proposed improvements. Initially, we discuss "Elitism", a widely extended modification in differential evolution algorithms. The following improvement, "Variable pattern length", is an adaptation of the two most effective improvements initially proposed by Cassar et al. [3] for a genetic algorithm optimizing a binary representation of a stimulation pattern. Finally, we discuss "Model down-sampling", an innovative approach proposed in this work to increase the computational efficiency of the optimization without compromising performance.

5.5.1. STATE OF THE ART IN APPLICATION-SPECIFIC MODIFICATIONS OF OPTIMIZATION ALGORITHMS FOR NEURAL STIMULATION

In different domains, it has been proven that application-specific modifications to the optimization methodology have the potential of boosting performance [97, 98]. Probably the most relevant work in the field of optimizing waveform parameters in neural stimulation applications is presented by Cassar et al. [3] where 5 different improvements to the standard Genetic Algorithm are presented and benchmarked. The application described in Cassar et al. [3] is considerably different and they focus on a binary representation of the waveform (presence or absence of a pulse). Additionally, their base algorithm is a Genetic Algorithm and not Differential Evolution algorithm. For these two reasons, only selected modifications will be included and they will need to be adapted to the specific requirements of our application.

One of the first modifications proposed is an application-specific pulse mutation where, instead of using the standard random mutation techniques presented by traditional genetic algorithms, the mutation is produced by adding, removing or moving pulses. The technique starts by randomly selecting the type of mutation to perform, then the location is randomly chosen and the mutation is performed. This process is repeated over a fixed number of desired mutations. Standard techniques bias the solution to an equal number of ones and zeros. This method solves the issue as there is an equal chance of increasing or reducing the frequency.

Secondly, instead of randomly generating new individuals of the population, the immigrants are generated by mating a parent from the current generation with a random immigrant. This leads to the generation of "competitive immigrants", which prevent the drop of fitness associated by completely random immigrants. Additionally, they propose an alternative immigrant generation technique based on a heuristic linking the number of pulses, the inter-pulse delays and the frequency of each inter-pulse delay with the fitness based on previous records. This information is used to generate "predictive immigrants".

An additional improvement proposed by Cassar et al. [3] is adjusting the length of the stimulation pattern as the generations progress. Initially, the length of the pattern

is short and the same pattern is repeated over the MRG simulation time. As optimization generations progress the pattern is increased in length allowing exploration of lower frequencies.

Finally, a jump-start technique is used to escape local optima. If the same maximum fitness is reported for 20 consecutive generations the ratios of immigrants and predictive immigrants are increased considerably with respect to the offspring to prioritize exploration overexploitation.

The improvements were extensively tested on several benchmark functions. The most effective improvement was the "predictive immigrants". The Pulse Mutation Method modification managed to reduce the variance, competitive immigrants reduced the number of poorly performing individuals and the variable pattern length also improved performance. Jump-start was arguably the least effective of the improvement.

The specific proposed improvements are tailored to a binary waveform representation representing the presence or absence of a pulse. In our application, we use continuous amplitudes which makes it hard to directly benefit from these modifications. Additionally Differential Evolution has some of these modifications implicitly implemented. For instance, the "competitive immigrants" improvement where the new immigrants are generated by mating a current parent with a random immigrant is implicit to the algorithm chosen, DE/best/1/bin, which uses the best individual in the population to generate all potential children. The jump-start technique, given its low performance, will not be incorporated. Additionally, the prevention of a stagnation in local optima is already achieved by adjusting the F and CR parameters dynamically as discussed in the section "Optimization parameters". The pulse mutation and "competitive immigrant" methods rely on the binary pulse codification and cannot be adapted. Given their simplicity yet notable improvement in the overall performance, variable pulse length and elitism will be analyzed and considered for inclusion.

5.5.2. ELITISM

In order to prevent the loss of the top performing individuals due to the stochastic nature of the generation and selection processes involved in optimization algorithms like PSO, GA or DE the principle of elitism is widely spread. The principle is simple: keep the top scoring individuals (the elite) in the population. The proportion of the elite with respect to the total stimulation can be adjusted to the specific application.

It is important to note that, in the base algorithm selected (DE/best/1/bin). elitism is already implicitly implemented. Firstly, the best individual is always used as the base for the crossover step. Additionally, in the selection process, each child is compared to its parent and the best one is selected. Nevertheless, it is still possible that some of the elites will not advance to the next generation. We implement elitism by bypassing the selection process for the top performing individuals in the generation. The children of the elite, which are then left without any individual to be compared with, will be compared with the worst performing individuals and their children. The best performing individual out of the 3 will advance to the next generation. Figure 5.6 shows the fitness comparison between different amounts of elitism. The addition of elitism leads to better performance. In particular, an elitism ratio of 10%, which coincides with the value used in similar applications [3], gives the best performance.

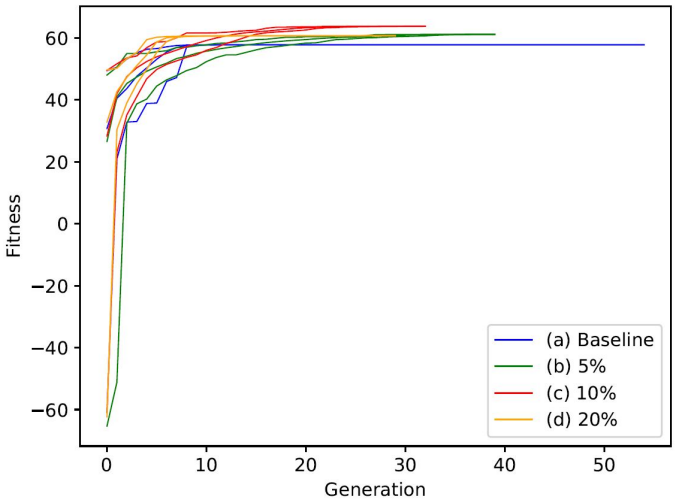

Figure 5.6: Performance comparison of different elitism rates (a) No elitism (b) 5% elitism (c) 10% elitism (d) 20% elitism

5.5.3. VARIABLE PATTERN LENGTH

The proposed waveform representation scheme can already accommodate a variable pattern length given that its frequency parameter determines the period and thus the length of the pattern. Nevertheless, only one period is stored. In order to fully incorporate the variable pattern length improvement, the number of periods stored by each individual needs to be increased as the optimization algorithm progresses. Experimental simulations show that a variable pattern that doubles every 40 generations improves the performance of the algorithm considerably as it allows for exploration of lower frequencies. Additionally, this modification has proven to be useful in escaping local optima and keeping enough variance in the population. One of the inconveniences of this approach is the increasingly large amount of data needed to characterize the waveform that which can slow down the algorithm and the storing processes.

5.5.4. MODEL DOWN-SAMPLING. AN INNOVATIVE APPROACH FOR SPEEDING UP COMPUTATIONALLY EXPENSIVE OPTIMIZATIONS

Given the high computation expenses of the MRG model, assessing the efficacy of the conduction block is the main bottleneck. The changes in the waveform between generations are subtle, especially as we approach the end of the simulation (exploitation phase) and they don't necessarily influence the block successfulness. This knowledge can be exploited by only determining the effectiveness of the conduction block once every N generations. We propose an adaptive block simulation period N that is low at the beginning of the optimization while the algorithm is in the exploration phase and it increases as the number of successful blocks in the generation increases when exploitation is predominant. This approach successfully guarantees the same performance while reducing the simulation time by a factor of $\frac{G \cdot N}{G+(N-1)}$, where N is the number of generations

elapsed between two complete evaluations of the model and G is the speed-up gain defined as the ratio between the complete and the partial model execution times. In our case, $G = 3$ and an $N = 4$ guarantees an overall speed-up of 2 which is already two-thirds of the hypothetical maximum. Choosing a low value prevents the population from drifting away to a point where no successful block can be achieved.

An alternative is to make N linearly dependent on the proportion of successful blocks in the population $RATIO_{blocked} = \frac{POP_{blocked}}{POP_{total}}$, where POP_{total} is the total population size and $POP_{blocked}$ is the total number of successful blocks in the population. Given their simplicity we propose the use of the following two functions:

$$N = \lceil K \cdot RATIO_{blocked} \rceil \tag{5.5}$$

$$N = \lceil K^{RATIO_{blocked}} \rceil \tag{5.6}$$

Additionally we could add a differential component by also factoring in the change in $RATIO_{blocked}$ over generations:

$$N_{next} = \lceil K_p \cdot RATIO_{blocked,g} + K_d \cdot \frac{(RATIO_{blocked,g} - RATIO_{blocked,g-N_{prev}})}{N_{prev}} \rceil \tag{5.7}$$

$$N = \lceil K_p^{RATIO_{blocked}} + K_d^{\frac{(RATIO_{blocked,g} - RATIO_{blocked,g-N_{prev}})}{N_{prev}}} \rceil M \tag{5.8}$$

Given the low speed-up gain G in our implementation, the adaptive schemes proposed do not prompt a considerable improvement over the constant N scheme. We predict that applications with a higher G will potentially benefit from the adaptive schemes presented.

While the presented approach follows the general philosophy of loosely evaluating the fitness function present in techniques such as fitness function approximation [99] or fitness inheritance [100] we have not identified any similar approach in literature and believe it to be a unique contribution to the field.

5.6. SOFTWARE IMPLEMENTATION AND HARDWARE RESOURCES

The Differential Evolution algorithm was implemented using the DEAP Python library which provides the basic platform needed to efficiently implement a wide range of stochastic optimization algorithms.

In order to speed up the optimization process, the fitness function evaluation, the most computationally expensive step in the process, was parallelized using the multiprocessing python library. The code can be run on any machine and the number of cores is adjusted dynamically for maximum efficiency. Nevertheless, the simulations presented in this thesis were run in the server cluster of the Intelligent System Group. Up to 64 cores were used to simultaneously run 64 different evaluations. Figure 5.7 shows the speed-up results.

5.7. CONCLUSION

In order to optimize the highly non-linear, discontinuous and non-differential models used, it is necessary to use stochastic swarm intelligence optimization algorithms.

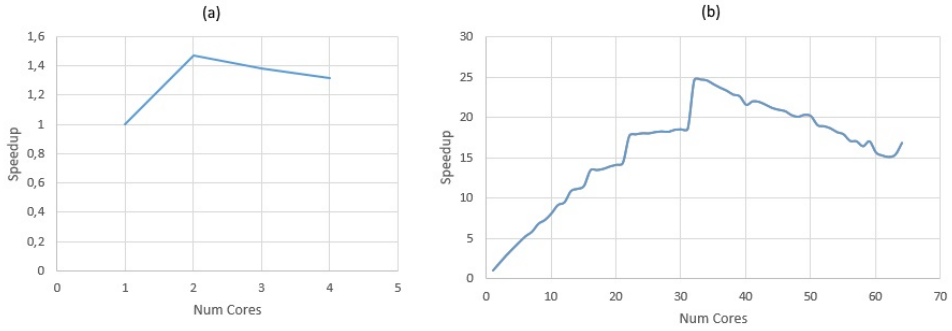

Figure 5.7: Speedup depending on the number of chores used. In each measurement, the simulation consisted on simulating the MRG model one time per chore used. The maximum speedup is achieved when using half of the available cores. (a) Using local machine Intel ® Core ™ i5-7200U CPU @ 2,5GHz with 4 cores and 8GB RAM(b) Using the "hopper" server in the INSY cluster Intel® Xeon® CPU E5-2620 V4 @ 2,10GHz 64 cores 256GB RAM

Among all alternatives, differential evolution (DE) has demonstrated reliability, robustness, ease of use, faster convergence and improved results. While PSO and GA have been used previously in the field of neural stimulation optimization, this is the first work using DE. The particular algorithm DE/best/1/bin has been chosen as it demonstrated superior performance over other alternatives.

The fitness function determines the performance of each waveform by combining two metrics: the presence or absence of a conduction block and the distance of the maximum and minimum values of the ETI voltage to the midpoint of the safe ETI window. By means of simulation, it was demonstrated that an exponential fitness function yields improved performance and faster convergence as anticipated in previous studies [91].

An orthogonal approach has been proposed for the waveform representation with the intention of ensuring fast convergence to the global optima. The proposed schemes allow for easy interpretation of the influence of each waveform parameter independently. The normalized cathodic and anodic pulses of the waveform, the amplitude, frequency, desired charge imbalance, and duty-cycle are stored separately. Nevertheless, experimental data has shown a much simpler waveform representation to be most suitable for the application. The best performing waveform representation consists of the complete waveform shape (no division between anodic and cathodic pulses), the amplitude and the frequency. Two main aspects have been identified as responsible for the improved performance of the simpler waveform representation. On the one hand, given that charge balance is not enforced, the solutions present a slight offset in the ETI voltage bringing the ETI voltage closer to the V_{safe} target. Additionally, the arbitrary waveform representation is not limited to waveforms with an anodic and a cathodic pulse, allowing the optimization algorithm to explore a wider search space.

The three optimization parameters of the DE algorithm have been adjusted to maximize performance and convergence speed. A population size NP of 256 is chosen as it is higher than double the dimensionality of the problem and is a multiple of the number of processors used, which maximized efficiency. In the selection of the scale factor, F and

crossover ratio CR an evolutionary approach demonstrated dominance over all other adaptive schemes tested. The two parameters are included in the genes of the individuals and are mutated along with the rest of the parameters to find the optimal solution.

Additionally, several improvements to the standard DE have been proposed. An elitism ratio of 10% has proven to obtain better results. Variable pattern, an improvement initially proposed by Cassar et al. [3], has proven to be useful in escaping local optima and keeping enough variance in the population. Other improvements proposed by Cassar et al. [3] have not been considered given the fact that they are either already implicitly implemented by the DE algorithm or not applicable in the continuous waveform optimization problem.

Finally, acknowledging the fact that the axonal model is the main bottleneck in computational terms, an improvement baptized as "model down-sampling" is presented. Model down-sampling consists on executing the axonal model to determine the effectiveness of the block only once every N generations. This technique manages to effectively double the execution speed of the optimization algorithm without compromising the accuracy. Several adaptive schemes for the down-sampling ratio N have been proposed but given the modest difference between the complete and partial execution times, they have not been adopted. We predict that problems in which such a ratio is larger (more computationally expensive axonal models or less computationally expensive ETI models) will benefit from such adaptive schemes. While the presented approach follows the general philosophy of loosely evaluating the fitness function present in techniques such as fitness function approximation [99] or fitness inheritance [100], we have not identified any similar approach in literature and believe it to be a unique contribution to the field.

In conclusion, DE/best/1/bin in combination with evolutionary adaptive parametrization, elitism, variable pattern, and model down-sampling has proven one of the most powerful tools in the optimization of waveforms for high-frequency nerve block applications.

6

RESULTING OPTIMAL STIMULATION WAVEFORM

6.1. STATE OF THE ART BASELINE

Before trying to find optimal stimulation waveforms, we will first establish a baseline by assessing the safety of the current state of the art. Most of the studies available focus on the use of square waveforms and sine-waves. In this first section, the block thresholds for these two types of waveforms in a frequency range between 2 and 20 kHz will be studied. The blocking threshold is defined as the minimum signal amplitude needed to achieve a successful block. Additionally, we propose the use of the ETI voltage threshold as a measure of waveform stimulation safety. The ETI voltage threshold is defined as the voltage window at the ETI when the threshold current is applied. These benchmarks will be used to assess the improvement in terms of electrochemical safety of the proposed waveforms.

A binary search algorithm is used to determine the block threshold for each stimulation waveform and frequency. In the classical algorithm, the model is evaluated at different amplitudes spaced with a given step size. When a transition from non-block to block is found, the step size is reduced by half and the direction of exploration is inverted to get closer to the solution. In order to speed up the search process, we propose a modification to the algorithm which can benefit from parallel computing. Initially, the amplitude range is defined between 0 and double the block threshold amplitude reported by Zhao et al. [55]. A total of 32 equally spaced samples in the range are taken and each processed by a different core. Once all the values have been evaluated the transition point in the range where the results go from non-blocked to blocked is determined. The two values where this transition occurs are taken as the edges of a new range to be divided into 32 new levels. The process is repeated until the absolute and relative accuracy requirements are met. The chosen absolute and relative accuracies are 0.1 mA and 1% respectively.

When reviewing the block threshold studies available in literature it is critical to an-

alyze the major discrepancies between Bhadra et al. [80] and Zhao et al. [55]. These two reference studies present highly dissonant results. Bhadra et al. [80] characterizes the nerve block using the MRG and predicts much lower block thresholds than Zhao et al. [55] who rely on the HH model. These differences are crucial given that the results reported by Zhao et al. [55] yield an increasing ETI voltage and thus a less safe stimulation as frequency increases, while the results given by Bhadra et al. 2007 [80] have the opposite effect, namely that higher frequencies lead to safer stimulation. Being able to understand where these differences come from will prove crucial in our modeling efforts.

To some degree, the differences are rooted in the fact that two different models are used. Nevertheless, the main point of divergence lays in the fact that two different axoplasm resistivities and myelin capacities are used. Bhadra et al. [80] use the standard MRG parameters, a myelin capacitance of 0.1 $\mu F/cm^2$ and axoplasmic resistivity of 0.7 Ω/cm^2 while Zhao et al. [55] use a myelin capacitance of 2 $\mu F/cm^2$ and axoplasmic resistivity of 1 Ω/cm^2. When using the values employed by Zhao et al. [55] their results can be closely replicated with the MRG model.

Figure 6.1 shows the block threshold values for a standard frequency range between 2kHz and 20kHz. Figure 6.1(TOP) shows the threshold block while Figure 6.1(BOTTOM) shows the ETI voltage window in such conditions. The two standard biphasic charge balanced waveforms (sinewave and squarewave) are evaluated using the two alternative parametrizations discussed earlier. These characterization results show that standard stimulation waveforms techniques are not completely free from irreversible reactions given that the resulting ETI potential windows span over the defined safe window of -0.25 to +0.55 V (marked in gray)[75]. Another point to note is that using the standard MRG parametrization of Bhadra et al. [80] the ETI window gets narrower as frequency increases, while in the case of the Zhao et al. [55] parametrization the opposite effect takes place. Waveforms with frequencies higher than 40 kHz did not consistently block the conduction. These limitations coincide with the values previously reported in literature for the MRG model [80]

Figures 6.2 and 6.3 further expand the characterization of state-of-the-art stimulation waveforms by analysing the effect of an inter-pulse delay. Increasing the length of the inter-pulse interval requires higher block thresholds and leads to slightly wider ETI threshold voltages. Waveforms with inter-pulse intervals greater than 60% of the total period did not successfully achieve nerve conduction block.

6.2. OPTIMAL WAVEFORM SHAPE

Figure 6.4 shows the top performing waveforms after a 200 generation run of the optimization algorithm for two different base frequencies (8 and 20 kHz). The resulting waveforms share several common traits such as a similar spectrum shape and a slight charge imbalance to bring the ETI voltage in the middle of the safe window. The results are compared to two baseline sine-waves with frequencies corresponding to the lower and upper limits of the blocking frequency range (2 kHz and 40kHz). As reported previously in literature [80] and verified in the model used in this study, sinusoidal signals lower than 2 kHz and higher than 40 kHz fail to achieve a reliable conduction block when using the MRG model. In order to ensure comparability of the results, the baseline sinewaves have the same signal power as the optimized waveforms and have a slight

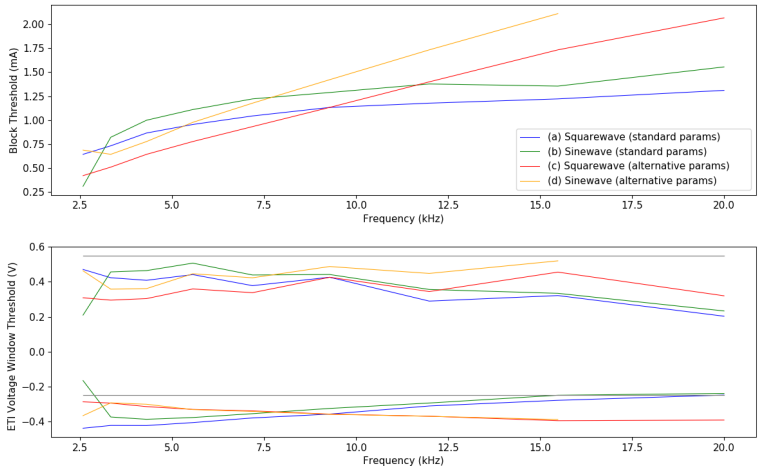

Figure 6.1: Threshold currents (TOP) and threshold ETI potential windows (BOTTOM) of standard stimulation waveforms (a) Charge-balanced squarewave using the standard MRG parametrization used in Bhadra et al. [80] (b) Charge-balanced sinewave using the standard MRG parametrization used in Bhadra et al. [80] (c) Charge-balanced squarewave using the alternative parametrization used in Zhao et al. [55] (d) Charge-balanced sinewave using the alternative parametrization used in Zhao et al. [55]

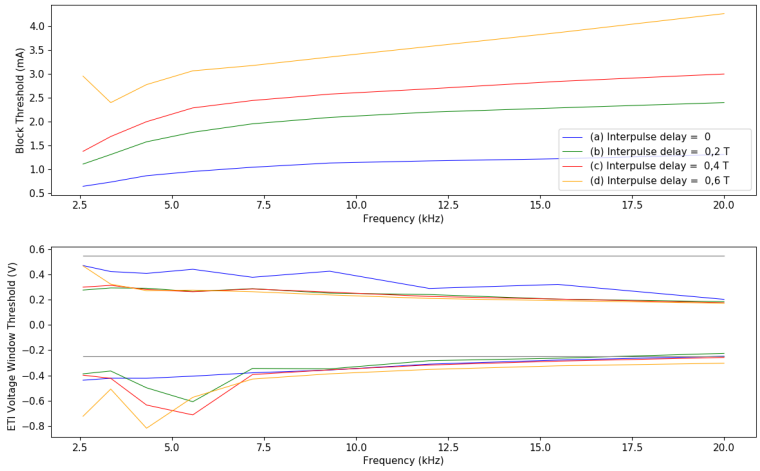

Figure 6.2: Influence of the interpulse interval on threshold currents (TOP) and threshold ETI potential windows (BOTTOM) using the standard model parametrization used in Bhadra et al. [80]. Increasing inter-pulse intervals lead to higher threshold currents and slightly worse ETI voltages (a) Charge-balanced squarewave with 0 interpulse interval. (b) Charge-balanced squarewave with an interpulse interval of 20% of the total period. (c) Charge-balanced squarewave with an interpulse interval of 40% of the total period. (d) Charge-balanced squarewave with an interpulse interval of 60% of the total period.

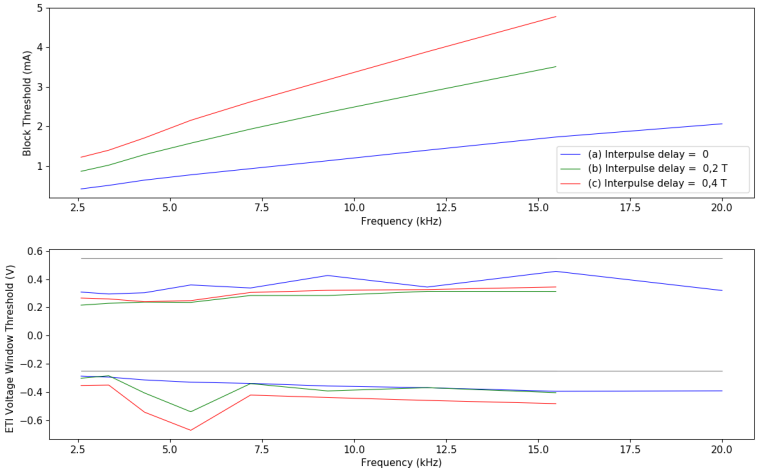

Figure 6.3: Influence of the interpulse interval on threshold currents (TOP) and threshold ETI potential windows (BOTTOM) using the standard model parametrization used in Zhao et al. [55]. Increasing inter-pulse intervals lead to higher threshold currents and slightly worse ETI voltages (a) Charge-balanced squarewave with a 0 interpulse interval. (b) Charge-balanced squarewave with an interpulse interval of 20% of the total period. (c) Charge-balanced squarewave with an interpulse interval of 40% of the total period.

charge imbalance to ensure a mean V_{ETI} of $0.15V$.

In order to assess the improvement on safety achieved, the safety margin (M) of the optimized waveform is compared to that of the baseline. For those waveforms leading to an ETI voltage within the safe stimulation limits ($-0.25V < V_{ETI} < 0.55V$) the safety margin (M) is defined as:

$$M = \frac{V_{safe,window} - (V_{ETI,max} - V_{ETI,min})}{V_{safe,window}} \tag{6.1}$$

Where $V_{ETI,max}$ and $V_{ETI,min}$ correspond to the maximum and minimum ETI voltage respectively and $V_{safe,window}$ corresponds to the difference between the upper and lower limits of the safe ETI potential window. In the case of platinum electrodes this value is $V_{safe,window} = 0.8V$ [74].

The 2 kHz baseline overflows the safe ETI window leading to unsafe stimulation. For a base frequency of 8 kHz, the obtained optimized waveform leads to an increase of 17.3% in the safety margin with respect to the 40 kHz baseline. For a base frequency of 20 kHz, the improvement is much more significant leading to an increase of 39.8% in the safety margin.

6.3. NOTES ON HARDWARE IMPLEMENTATION

The non-standard waveforms obtained set high implementation requirements. One possible hardware implementation direction is to reduce the obtained optimal waveform to its main harmonics. Only the DC component, the fundamental frequency and a set of N harmonics are used to generate the complex waveform dropping the rest of the

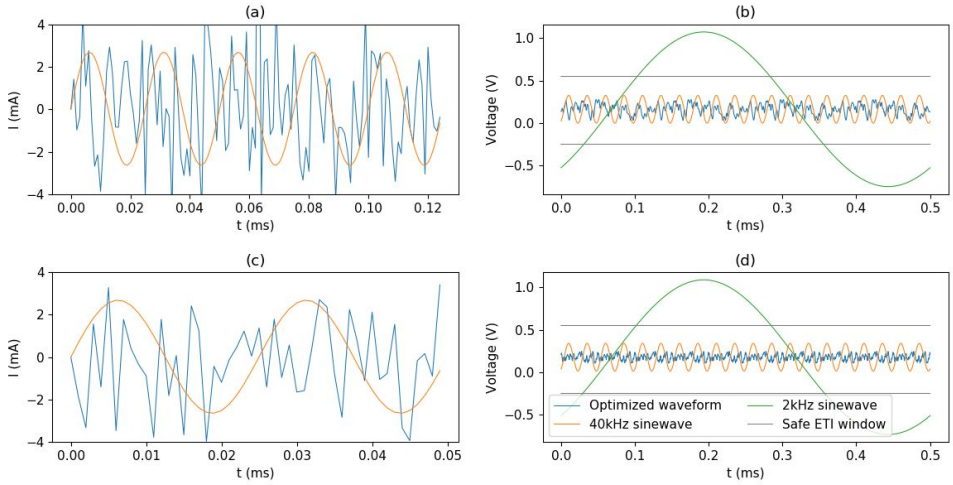

Figure 6.4: Optimal waveform after 200 generations for two different base frequencies using the arbitrary waveform representation. Two baseline sinusoidal stimulation waveforms with the same power and the required offset to ensure a mean V_{ETI} of $0.15V$ are added for comparison. The frequencies of the baseline sinusoids correspond to the lower and upper blocking limits of the MRG model 2 kHz and 40 kHz (a) Period of the optimal waveform with a base frequency of 8 kHz compared to a baseline sinewave of 40 kHz (b) V_{ETI} response of the optimal waveform with a base frequency of 8 kHz compared to that of the two baseline sinusoids (2 kHz and 40 kHz). The optimized waveform shows a maximum ETI voltage of $V_{ETI} = 276mV$ and a minimum voltage of $V_{ETI,min} = 31mV$ which implies a safety margin improvement of 17.3% with respect to the 40 kHz baseline. The 2 kHz baseline overflows the safe ETI window leading to unsafe stimulation. (c) Period of the optimal waveform with a base frequency of 20 kHz compared to a baseline sinewave of 40 kHz (d) V_{ETI} response of the optimal waveform with a base frequency of 20 kHz compared to that of the two baseline sinusoids (2 kHz and 40 kHz). The optimized waveform shows a maximum ETI voltage of $V_{ETI} = 246mV$ and a minimum voltage of $V_{ETI,min} = 107mV$ which implies a safety margin improvement of 39.8% with respect to the 40 kHz baseline. The 2 kHz baseline overflows the safe ETI window leading to unsafe stimulation.

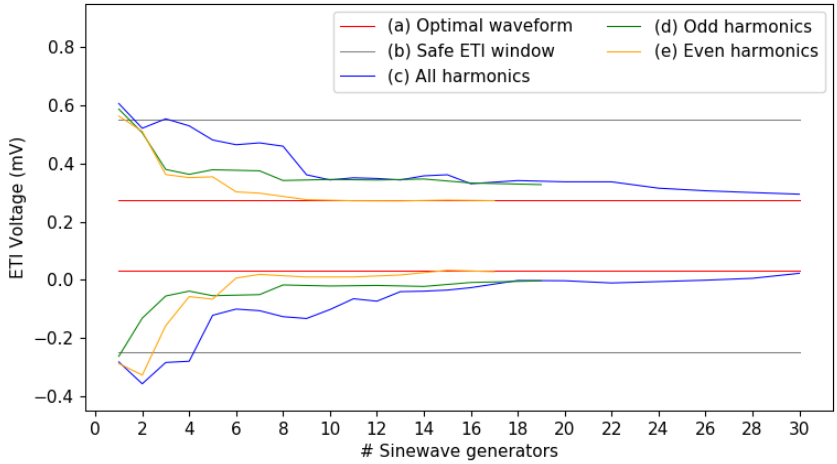

Figure 6.5: ETI voltage window of the three waveform simplification approaches proposed depending on the number of sinewave generators needed. For each alternative, the top line represents the maximum ETI voltage while the bottom one represents the minimum ETI voltage. The optimal waveform presented in Figure 6.4c is used as the base. Each of the simplification waveforms has the same power as the original one and has the needed charge imbalance to ensure a mean V_{ETI} of $0.15V$. (a) Optimal waveform: ETI window of the optimized waveform presented in Figure 6.4c (b) Safe ETI window [74] (c) All harmonics: The original signal is simplified by only taking the DC component, the fundamental frequency and a set of harmonics. Around 30 sinewave generators are needed to achieve the ETI window levels of the optimal waveform (d) Odd harmonics: The original signal is simplified by only taking the DC component, the fundamental frequency and a set of N odd harmonics. (e) Even harmonics: The original signal is simplified by only taking the DC component, the fundamental frequency and a set of N even harmonics. The convergence is faster and only 6 to 8 sinewave generators are needed to reach the ETI voltage levels of the optimal waveform

spectral information. In its hardware implementation, each harmonic would be generated with a different sinewave generator. Figure 6.5 shows the resulting ETI voltage depending on the number of sine-wave generators needed in its hardware realization. This approach would require a total of 30 sinusoids to achieve the same ETI voltage levels as the optimized waveform. While this is already an improvement it is still hard to realize. As an alternative, two additional simplification approaches have been proposed taking only the odd and even harmonics respectively. By following these approaches the number of sine-wave generators required to cover the same bandwidth is reduced by half with respect to the approach using all harmonics. Using only the odd harmonics represents an improvement on the lower end but it does not relax the requirements to achieve when trying to achieve the optimal ETI voltage levels. Using only the even harmonics, on the other hand, manages to effectively bring down the number of required sine-wave generators down to only 6. It is important to state that, none of these simplifications affect the efficacy of the block since regardless of the number of harmonics taken they all manage to achieve a successful conduction block.

7

CONCLUSION

This thesis presents a novel computational approach for finding optimal waveform patterns for minimized electrochemical damage in high-frequency conduction block applications. While the main focus has been the stimulation of the pudendal nerve for treatment of non-neurogenic urinary retention, the obtained results are applicable to any peripheral nerves with a similar anatomical constitution. The MRG axonal model is combined with an electrode-tissue interface (ETI) model based on in vivo experimental data to obtain a computational model capable of assessing the efficacy and electrochemical safety of a given stimulation waveform. This model is coupled to a Differential Evolution (DE) algorithm to find the optimal stimulation waveform that ensures a reliable conduction block and a minimal ETI voltage. This is a unique approach in literature, given that no previous attempts had been done in the exploration of non-regular waveforms for high-frequency optimization block. Additionally, it is the first attempt to include an experimentally parametrized ETI model with the intention of assessing acute electrochemical safety. Finally, while Genetic Algorithms, Particle Swarm Optimization (PSO) and other stochastic swarm optimization algorithms have been used in the past in the field of neural stimulation optimization, it is the first time that Differential Evolution (DE) algorithms are used.

Chapter 2 showed that urinary retention can have neurogenic and non-neurogenic causes. In the treatment of non-neurogenic urinary retention electrical stimulation stands out as a fast, reliable, safe and highly selective option. The electrochemical safety of high-frequency stimulation can potentially be improved by means of non-standard stimulation waveforms.

In its pass through the pudendal canal, the pudendal nerve has an elliptical cross-section with an effective diameter of $3.2mm$, it contains dozens of fascicles which are composed of several myelinated axons with diameters as small as $5\ \mu m$.

In Chapter 3 the three major acute stimulation damage mechanisms related to electrical stimulation were identified (hyper-activation, electroporation, and electrochemical activation) and electrochemical activation was chosen as the main focus of this thesis. The electrode-tissue interface (ETI) models the non-linear charge transfer processes

during stimulation. Electrochemical safety is ensured by minimizing the charge injection through non-reversible processes and ensuring that the ETI voltage is kept within the safe ETI window ($-0.25 < V_{ETI} < 0.55$)). An experimentally parametrized ETI model is used in order to assess reversible and non-reversible currents as well as the voltage across the ETI.

Small charge imbalances lead to safer stimulation as the small offset introduced can set the ETI voltage in the center of the non-symmetrical limits of the safe ETI window. Additionally, higher frequencies might not necessarily lead to safer stimulation given the higher amplitudes needed to achieve a successful conduction block.

In Chapter 4 the main computational axonal models were compared with a special focus on its suitability for high-frequency block modeling. The McIntyre, Richardson, and Grill (MRG) nerve axonal model was selected given its suitability for high-frequency block modeling, the fact that is based partially on human data and its extensive use in previous literature. The original NEURON model published by their authors was adapted and interfaced with a Python script.

Chapter 5 presents the design of the optimization algorithm used. In order to optimize the highly non-linear, discontinuous and non-differential models used, it is necessary to use stochastic swarm intelligence optimization algorithms. Among all alternatives, differential evolution (DE) has demonstrated reliability, robustness, ease of use and faster convergence. An exponential function calculated using the presence of a conduction block and the distance of the ETI voltage to the midpoint of the safe ETI window is used to assess the fitness of each waveform. An arbitrary waveform representation has shown the best performance over more constrained alternatives as it allows the exploration of a wider portion of the search space. Different modifications were proposed to the original DE algorithm. DE/best/1/bin in combination with evolutionary adaptive parametrization, elitism, variable pattern and a new contribution named "model downsampling", has proven one of the most powerful tools in the optimization of waveforms for high-frequency nerve block applications.

Finally, chapter 6 presented several optimized waveform shapes ensuring a successful high-frequency conduction block with 39.8% safety margin improvement with respect to the safest standard stimulation pattern. This proves that non-standard stimulation waveforms with a slight charge imbalance can be used for safer stimulation.

In conclusion, the developed platform has successfully demonstrated its ability to exploit non-standard patterns to find electrochemically safer waveforms for efficacious conduction block of the pudendal nerve.

7.1. CONTRIBUTIONS

One of the main contributions of this thesis is that, while many attempts have been conducted aiming at optimizing neural stimulation waveforms for action potential elicitation, this is the first attempt to explore non-standard waveforms for high-frequency nerve conduction block by means of computer optimization. Additionally, none of the previous studies focused on the exploration of acute electrochemical safety. This study, therefore, opens a new research niche with a promising future.

It is also the first attempt of applying DE in the field of neural stimulation optimization, an algorithm that has proven to outperform other alternatives such as PSO or GA

in other fields and has demonstrated reliability, robustness, ease of use and fast convergence for this particular application.

The standard DE algorithm has been improved and adapted to the specific application by including evolutionary adaptive parametrization, elitism, and variable pattern. Additionally, a novel improvement baptized as "model down-sampling" has been presented. Model down-sampling consists on only executing the axonal model to determine the effectiveness of the block once every N generations. This technique manages to effectively double the execution speed of the optimization algorithm without compromising accuracy. While the presented approach follows the general philosophy of loosely evaluating the fitness function present in techniques such as fitness function approximation [99] or fitness inheritance [100] we have not identified any similar approach in literature and believe it to be a unique contribution to the field.

Another key contribution is the obtained optimal stimulation waveform which ensures a successful high-frequency conduction block with 39.8% safety margin improvement with respect to the safest standard stimulation pattern.

Finally, one of the most substantial contributions is the development of a unique platform to conduct future research in the field of high-frequency stimulation. The platform combines an axonal model to determine the efficacy of the conduction block, an electrode-tissue interface model to assess the electrochemical safety and an optimization algorithm. This unique optimization platform can be adapted to tackle a wider diversity of optimization problems.

7.2. FUTURE WORK

Firstly, given that this is a simulation study relying on computational models it is necessary to clinically validate the obtained optimal waveforms.

This study focused on minimizing electrochemical damage and did not take into account other sources of damage such as electroporation or neural hyperactivity. The low ETI voltages achieved are far from the electroporation dangerous levels. Nevertheless, more research needs to be done on neural hyperactivity and the ETI model used could be complemented with a neural hyperactivity model in future research.

The ETI is highly dependent on electrode and tissue properties. The ETI model used corresponds to platinum cuff electrodes. For alternative electrode types, an experimental ETI characterization is advised. These parameters would then be included in the model to recompute the optimal waveforms. Additionally, the ETI experiences notable changes over time. Long-term studies of the degradation of the ETI are needed and should be included in the model in order to find stimulation waveforms that can compensate for them. Alternatively, given that such studies are scarce, a Montecarlo simulation could be used to stochastically alter each of the parameters of the current ETI model. This would allow conducting a tolerance and adaptability study.

Several approaches have been proposed to cope with the high computational expenses of the axonal model used, such as multi-core parallel programming or "model down-sampling". In order to improve the computation speed even further, one could consider GPU acceleration. The GPU compatibility of the NEURON software is still under development which means that the MRG model should be reimplemented on an alternative programming environment with GPU acceleration capabilities. Currently, the

novel improvement "model down-sampling" presented in Chapter 5, uses a constant down-sampling ratio given the modest difference between the complete and partial execution times. We predict that problems in which such ratio is larger (more computationally expensive axonal models or less computationally expensive ETI models) will benefit from an adaptive down-sampling ratio leading to higher speed-ups. Ultimately, the MRG axonal model used could be simplified or linearized around an operation point.

Including other modifications presented by Cassar et al. [3] could be another line to pursue in an attempt to further improving the performance of the optimization algorithm. Special interest lays in the best performing improvement, "predictive immigrants". In such technique, relevant information of the best performing individuals in previous generations is used to generate new individuals for the next generation. The metrics used originally (number of pulses, inter-pulse delays and recurring frequency of each interpulse delay) are only defined in the binary representation scheme used by Cassar et al. [3] and new metrics relevant to a continuous waveform representation should be proposed.

The obtained optimal waveforms are difficult to realize in commercially available stimulators. One could use a more constrained waveform representation in the optimization algorithm to only explore waveforms that can be realized by the stimulator to be used. As an example, the waveforms could be limited to square-waves with only a few varying parameters such as the inter-pulse delay or the cathodic and anodic pulses amplitude and duration.

From a circuit design perspective, a clear line for future work is the design of new stimulation techniques and devices able to use the optimal stimulation waveforms found. This work already pointed out that a harmonic simplification of the obtained optimal waveform could potentially reduce the hardware implementation requirements burden. In particular, the reduction of the waveform to its DC component, fundamental frequency, and even harmonics proved to only require 6 sine-wave generators to achieve the same electrochemical safety levels as the optimal waveform.

Finally, the developed optimization tool opens the door to the exploration of many different optimization problems in the field of high-frequency stimulation. The fitness function could be adapted to minimize aspects such as power consumption or the onset response. Additionally, the electrode configuration and location could also be optimized.

BIBLIOGRAPHY

REFERENCES

[1] A. Boger, N. Bhadra, and K. J. Gustafson, "Bladder voiding by combined high frequency electrical pudendal nerve block and sacral root stimulation," *Neurourology and urodynamics*, vol. 27, no. 5, pp. 435–439, 2008.

[2] M. Van Dongen and W. Serdijn, *Design of Efficient and Safe Neural Stimulators: A Multidisciplinary Approach*. Springer, 2016.

[3] I. R. Cassar, N. D. Titus, and W. M. Grill, "An improved genetic algorithm for designing optimal temporal patterns of neural stimulation," *Journal of neural engineering*, vol. 14, no. 6, p. 066013, 2017.

[4] M. B. Chancellor and A. C. Diokno, *The Underactive Bladder*. Springer, 2016.

[5] Y.-H. Chang, J. J.-Y. Siu, P.-J. Hsiao, C.-H. Chang, and E. C.-L. Chou, "Review of underactive bladder," *Journal of the Formosan Medical Association*, 2017.

[6] F. Plotti, R. Angioli, M. A. Zullo, M. Sansone, T. Altavilla, E. Antonelli, R. Montera, P. Damiani, and P. B. Panici, "Update on urodynamic bladder dysfunctions after radical hysterectomy for cervical cancer," *Critical reviews in oncology/hematology*, vol. 80, no. 2, pp. 323–329, 2011.

[7] C. Maurer, K. Z'graggen, P. Renzulli, M. Schilling, P. Netzer, and M. Büchler, "Total mesorectal excision preserves male genital function compared with conventional rectal cancer surgery," *British journal of surgery*, vol. 88, no. 11, pp. 1501–1505, 2001.

[8] F. Stocchi, A. Carbone, M. Inghilleri, A. Monge, S. Ruggieri, A. Berardelli, and M. Manfredi, "Urodynamic and neurophysiological evaluation in parkinson's disease and multiple system atrophy.," *Journal of Neurology, Neurosurgery & Psychiatry*, vol. 62, no. 5, pp. 507–511, 1997.

[9] L. E. Medina Daza, *Quantitative Analysis of Kilohertz-Frequency Neurostimulation*. PhD thesis, 2016.

[10] B. F. Blok, "Sacral neuromodulation for the treatment of urinary bladder dysfunction: mechanism of action and future directions," *Bioelectronics in Medicine*, vol. 1, no. 1, pp. 85–94, 2018.

[11] X.-j. Feng, B. Greenwald, H. Rabitz, E. Shea-Brown, and R. Kosut, "Toward closed-loop optimization of deep brain stimulation for parkinson's disease: concepts and lessons from a computational model," *Journal of neural engineering*, vol. 4, no. 2, p. L14, 2007.

[12] A. Wongsarnpigoon and W. M. Grill, "Energy-efficient waveform shapes for neural stimulation revealed with a genetic algorithm," *Journal of neural engineering*, vol. 7, no. 4, p. 046009, 2010.

[13] A. R. Kent and W. M. Grill, "Model-based analysis and design of nerve cuff electrodes for restoring bladder function by selective stimulation of the pudendal nerve," *Journal of neural engineering*, vol. 10, no. 3, p. 036010, 2013.

[14] D. T. Brocker, B. D. Swan, R. Q. So, D. A. Turner, R. E. Gross, and W. M. Grill, "Optimized temporal pattern of brain stimulation designed by computational evolution," *Science translational medicine*, vol. 9, no. 371, p. eaah3532, 2017.

[15] E. Peña, S. Zhang, S. Deyo, Y. Xiao, and M. D. Johnson, "Particle swarm optimization for programming deep brain stimulation arrays," *Journal of neural engineering*, vol. 14, no. 1, p. 016014, 2017.

[16] J. P. Giuffrida and P. E. Crago, "Functional restoration of elbow extension after spinal-cord injury using a neural network-based synergistic fes controller," *IEEE Transactions on Neural Systems and Rehabilitation Engineering*, vol. 13, no. 2, pp. 147–152, 2005.

[17] K. L. Kilgore and N. Bhadra, "Reversible nerve conduction block using kilohertz frequency alternating current," *Neuromodulation: Technology at the Neural Interface*, vol. 17, no. 3, pp. 242–255, 2014.

[18] E. N. Marieb and K. Hoehn, *Human anatomy & physiology*. Pearson Education, 2007.

[19] T. L. Burney, M. Senapti, S. Desai, S. Choudhary, and G. H. Badlani, "Acute cerebrovascular accident and lower urinary tract dysfunction: a prospective correlation of the site of brain injury with urodynamic findings," *The Journal of urology*, vol. 156, no. 5, pp. 1748–1750, 1996.

[20] S. E. Litwiller, E. M. Frohman, and P. E. Zimmern, "Multiple sclerosis and the urologist," *The Journal of urology*, vol. 161, no. 3, pp. 743–757, 1999.

[21] J. Groen, J. Pannek, D. C. Diaz, G. Del Popolo, T. Gross, R. Hamid, G. Karsenty, T. M. Kessler, M. Schneider, B. Blok, *et al.*, "Summary of european association of urology (eau) guidelines on neuro-urology," *European urology*, vol. 69, no. 2, pp. 324–333, 2016.

[22] J. Jamison, S. Maguire, and J. McCann, "Catheter policies for management of long term voiding problems in adults with neurogenic bladder disorders," *The Cochrane Library*, 2013.

[23] Y. A. Patel and R. J. Butera, "Challenges associated with nerve conduction block using kilohertz electrical stimulation," *Journal of neural engineering*, vol. 15, no. 3, p. 031002, 2018.

[24] S. Fribance, J. Wang, J. R. Roppolo, W. C. de Groat, and C. Tai, "Axonal model for temperature stimulation," *Journal of computational neuroscience*, vol. 41, no. 2, pp. 185–192, 2016.

[25] D. E. Beck, P. L. Roberts, T. J. Saclarides, A. J. Senagore, M. J. Stamos, and Y. Nasseri, *The ASCRS textbook of colon and rectal surgery*. Springer Science & Business Media, 2011.

[26] P. A. Maldonado, K. Chin, A. A. Garcia, and M. M. Corton, "Anatomic variations of pudendal nerve within pelvis and pudendal canal: clinical applications," *American journal of obstetrics and gynecology*, vol. 213, no. 5, pp. 727–e1, 2015.

[27] K. J. Gustafson, P. F. Zelkovic, A. H. Feng, C. E. Draper, D. R. Bodner, and W. M. Grill, "Fascicular anatomy and surgical access of the human pudendal nerve," *World journal of urology*, vol. 23, no. 6, pp. 411–418, 2005.

[28] P. Malmivuo, J. Malmivuo, and R. Plonsey, *Bioelectromagnetism: principles and applications of bioelectric and biomagnetic fields*. Oxford University Press, USA, 1995.

[29] D. Boërio, J. Hogrel, A. Créange, and J. Lefaucheur, "Méthodes et intérêt clinique de la mesure de la période réfractaire nerveuse périphérique chez l'homme," *Neurophysiologie Clinique/Clinical Neurophysiology*, vol. 34, no. 6, pp. 279–291, 2004.

[30] Y. Avissar, J. Choi, J. DeSaix, V. Jurukovski, R. Wise, and C. Rye, *Biology*. OpenStax, 2013.

[31] A. L. Hodgkin and A. F. Huxley, "A quantitative description of membrane current and its application to conduction and excitation in nerve," *The Journal of physiology*, vol. 117, no. 4, pp. 500–544, 1952.

[32] B. Frankenhaeuser and A. Huxley, "The action potential in the myelinated nerve fibre of xenopus laevis as computed on the basis of voltage clamp data," *The Journal of Physiology*, vol. 171, no. 2, pp. 302–315, 1964.

[33] S. Chiu, J. Ritchie, R. Rogart, and D. Stagg, "A quantitative description of membrane currents in rabbit myelinated nerve.," *The Journal of physiology*, vol. 292, no. 1, pp. 149–166, 1979.

[34] J. R. Schwarz, G. Reid, and H. Bostock, "Action potentials and membrane currents in the human node of ranvier," *Pflügers Archiv*, vol. 430, no. 2, pp. 283–292, 1995.

[35] C. C. McIntyre, A. G. Richardson, and W. M. Grill, "Modeling the excitability of mammalian nerve fibers: influence of afterpotentials on the recovery cycle," *Journal of neurophysiology*, vol. 87, no. 2, pp. 995–1006, 2002.

[36] J. Couto and W. M. Grill, "Kilohertz frequency deep brain stimulation is ineffective at regularizing the firing of model thalamic neurons," *Frontiers in computational neuroscience*, vol. 10, p. 22, 2016.

[37] S. H. Weinberg, "High-frequency stimulation of excitable cells and networks," *PLoS One*, vol. 8, no. 11, p. e81402, 2013.

[38] F. Rattay, "High frequency electrostimulation of excitable cells," *Journal of theoretical biology*, vol. 123, no. 1, pp. 45–54, 1986.

[39] M. Y. Woo and B. Campbell, "Asynchronous firing and block of peripheral nerve conduction by 20 kc alternating current.," *Bulletin of the Los Angeles Neurological Society*, vol. 29, p. 87, 1964.

[40] J. Miles, K. Kilgore, N. Bhadra, and E. Lahowetz, "Effects of ramped amplitude waveforms on the onset response of high-frequency mammalian nerve block," *Journal of neural engineering*, vol. 4, no. 4, p. 390, 2007.

[41] M. Gerges, E. L. Foldes, D. M. Ackermann, N. Bhadra, N. Bhadra, and K. L. Kilgore, "Frequency-and amplitude-transitioned waveforms mitigate the onset response in high-frequency nerve block," *Journal of neural engineering*, vol. 7, no. 6, p. 066003, 2010.

[42] E. L. Foldes, D. M. Ackermann, N. Bhadra, and K. L. Kilgore, "Counted cycles method to quantify the onset response in high-frequency peripheral nerve block," in *Engineering in Medicine and Biology Society, 2009. EMBC 2009. Annual International Conference of the IEEE*, pp. 614–617, IEEE, 2009.

[43] D. M. Ackermann, N. Bhadra, E. L. Foldes, X.-F. Wang, and K. L. Kilgore, "Effect of nerve cuff electrode geometry on onset response firing in high-frequency nerve conduction block," *IEEE Transactions on Neural Systems and Rehabilitation Engineering*, vol. 18, no. 6, pp. 658–665, 2010.

[44] N. Bhadra, E. L. Foldes, D. M. Ackermann, and K. L. Kilgore, "Reduction of the onset response in high frequency nerve block with amplitude ramps from non-zero amplitudes," in *Engineering in Medicine and Biology Society, 2009. EMBC 2009. Annual International Conference of the IEEE*, pp. 650–653, IEEE, 2009.

[45] N. Bhadra, T. Vrabec, N. Bhadra, and K. Kilgore, "Response of peripheral nerve to high frequency alternating current (hfac) nerve block applied for long durations," in *Neural Interface Conference*, 2012.

[46] B. R. Bowman and D. R. McNeal, "Response of single alpha motoneurons to high-frequency pulse trains," *Stereotactic and Functional Neurosurgery*, vol. 49, no. 3, pp. 121–138, 1986.

[47] X. Zhang, J. R. Roppolo, W. C. De Groat, and C. Tai, "Simulation analysis of conduction block in myelinated axons induced by high-frequency biphasic rectangular pulses," *IEEE Transactions on Biomedical Engineering*, vol. 53, no. 7, pp. 1433–1436, 2006.

[48] C. Tai, W. C. de Groat, and J. R. Roppolo, "Simulation of nerve block by high-frequency sinusoidal electrical current based on the hodgkin-huxley model," *IEEE*

Transactions on Neural Systems and Rehabilitation Engineering, vol. 13, no. 3, pp. 415–422, 2005.

[49] K. L. Kilgore and N. Bhadra, "Nerve conduction block utilising high-frequency alternating current," *Medical and Biological Engineering and Computing*, vol. 42, no. 3, pp. 394–406, 2004.

[50] R. P. Williamson and B. J. Andrews, "Localized electrical nerve blocking," *IEEE Transactions on Biomedical Engineering*, vol. 52, no. 3, pp. 362–370, 2005.

[51] D. M. Ackermann, N. Bhadra, M. Gerges, and P. J. Thomas, "Dynamics and sensitivity analysis of high-frequency conduction block," *Journal of neural engineering*, vol. 8, no. 6, p. 065007, 2011.

[52] N. Bhadra, N. Bhadra, K. Kilgore, and K. J. Gustafson, "High frequency electrical conduction block of the pudendal nerve," *Journal of neural engineering*, vol. 3, no. 2, p. 180, 2006.

[53] N. Bhadra and K. L. Kilgore, "High-frequency electrical conduction block of mammalian peripheral motor nerve," *Muscle & Nerve: Official Journal of the American Association of Electrodiagnostic Medicine*, vol. 32, no. 6, pp. 782–790, 2005.

[54] Y. A. Patel and R. J. Butera, "Differential fiber-specific block of nerve conduction in mammalian peripheral nerves using kilohertz electrical stimulation," *Journal of neurophysiology*, vol. 113, no. 10, pp. 3923–3929, 2015.

[55] S. Zhao, G. Yang, J. Wang, J. R. Roppolo, W. C. de Groat, and C. Tai, "Conduction block in myelinated axons induced by high-frequency (khz) non-symmetric biphasic stimulation," *Frontiers in computational neuroscience*, vol. 9, p. 86, 2015.

[56] C.-W. Peng, J.-J. J. Chen, C.-C. K. Lin, P. W.-F. Poon, C.-K. Liang, and K.-P. Lin, "High frequency block of selected axons using an implantable microstimulator," *Journal of neuroscience methods*, vol. 134, no. 1, pp. 81–90, 2004.

[57] B. Howell, *Design of Electrodes for Efficient and Selective Electrical Stimulation of Nervous Tissue*. PhD thesis, 2015.

[58] W. F. Agnew, D. B. McCreery, T. G. Yuen, and L. A. Bullara, "Histologic and physiologic evaluation of electrically stimulated peripheral nerve: considerations for the selection of parameters," *Annals of biomedical engineering*, vol. 17, no. 1, pp. 39–60, 1989.

[59] W. Agnew, D. McCreery, T. Yuen, and L. Bullara, "Local anaesthetic block protects against electrically-induced damage in peripheral nerve," *Journal of biomedical engineering*, vol. 12, no. 4, pp. 301–308, 1990.

[60] D. R. Merrill, M. Bikson, and J. G. Jefferys, "Electrical stimulation of excitable tissue: design of efficacious and safe protocols," *Journal of neuroscience methods*, vol. 141, no. 2, pp. 171–198, 2005.

[61] S. F. Cogan, K. A. Ludwig, C. G. Welle, and P. Takmakov, "Tissue damage thresholds during therapeutic electrical stimulation," *Journal of neural engineering*, vol. 13, no. 2, p. 021001, 2016.

[62] A. Butterwick, A. Vankov, P. Huie, Y. Freyvert, and D. Palanker, "Tissue damage by pulsed electrical stimulation," *IEEE Transactions on Biomedical Engineering*, vol. 54, no. 12, pp. 2261–2267, 2007.

[63] J. C. Weaver and Y. A. Chizmadzhev, "Theory of electroporation: a review," *Bioelectrochemistry and bioenergetics*, vol. 41, no. 2, pp. 135–160, 1996.

[64] B. Mercadal, C. B. Arena, R. V. Davalos, and A. Ivorra, "Avoiding nerve stimulation in irreversible electroporation: a numerical modeling study," *Physics in Medicine & Biology*, vol. 62, no. 20, p. 8060, 2017.

[65] T. Rose and L. Robblee, "Electrical stimulation with pt electrodes. viii. electrochemically safe charge injection limits with 0.2 ms pulses (neuronal application)," *IEEE Transactions on Biomedical Engineering*, vol. 37, no. 11, pp. 1118–1120, 1990.

[66] J. C. Lilly, J. R. Hughes, E. C. Alvord Jr, and T. W. Galkin, "Brief, noninjurious electric waveform for stimulation of the brain.," *Science*, 1955.

[67] W. F. Agnew and D. B. McCreery, "Considerations for safety with chronically implanted nerve electrodes," *Epilepsia*, vol. 31, no. s2, 1990.

[68] R. V. Shannon, "A model of safe levels for electrical stimulation," *IEEE Transactions on Biomedical Engineering*, vol. 39, no. 4, pp. 424–426, 1992.

[69] A. J. Bard, L. R. Faulkner, J. Leddy, and C. G. Zoski, *Electrochemical methods: fundamentals and applications*, vol. 2. wiley New York, 1980.

[70] S. Khan, S. A. Rizvi, and S. Urooj, "Equivalent circuit modelling using electrochemical impedance spectroscopy for different materials of sofc," in *Computing for Sustainable Global Development (INDIACom), 2016 3rd International Conference on*, pp. 1563–1567, IEEE, 2016.

[71] X. F. Wei and W. M. Grill, "Impedance characteristics of deep brain stimulation electrodes in vitro and in vivo," *Journal of neural engineering*, vol. 6, no. 4, p. 046008, 2009.

[72] F. Kolbl, J. Sabatier, G. N'Kaoua, F. Naudet, E. Faggiani, A. Benazzouz, S. Renaud, and N. Lewis, "Characterization of a non linear fractional model of electrode-tissue impedance for neuronal stimulation," in *Biomedical Circuits and Systems Conference (BioCAS), 2013 IEEE*, pp. 338–341, 2013.

[73] M. Sawan, Y. Laaziri, F. Mounaim, E. Elzayat, J. Corcos, and M. Elhilali, "Electrode–tissues interface: Modeling and experimental validation," *Biomedical materials*, vol. 2, no. 1, p. S7, 2007.

[74] E. Hudak, J. Mortimer, and H. Martin, "Platinum for neural stimulation: voltammetry considerations," *Journal of neural engineering*, vol. 7, no. 2, p. 026005, 2010.

[75] E. M. Hudak, *Electrochemical evaluation of platinum and diamond electrodes for neural stimulation*. PhD thesis, Case Western Reserve University, 2011.

[76] T. Eriksson, *A Finite Element Study of the Electrode Configuration for Nerve Conduction Block*. Skolan för datavetenskap och kommunikation, Kungliga Tekniska högskolan, 2008.

[77] J. Wang, B. Shen, J. R. Roppolo, W. C. de Groat, and C. Tai, "Influence of frequency and temperature on the mechanisms of nerve conduction block induced by high-frequency biphasic electrical current," *Journal of computational neuroscience*, vol. 24, no. 2, pp. 195–206, 2008.

[78] N. T. Carnevale and M. L. Hines, *The NEURON book*. Cambridge University Press, 2006.

[79] S. Joucla and B. Yvert, "Modeling extracellular electrical neural stimulation: from basic understanding to mea-based applications," *Journal of Physiology-Paris*, vol. 106, no. 3-4, pp. 146–158, 2012.

[80] N. Bhadra, E. A. Lahowetz, S. T. Foldes, and K. L. Kilgore, "Simulation of high-frequency sinusoidal electrical block of mammalian myelinated axons," *Journal of computational neuroscience*, vol. 22, no. 3, pp. 313–326, 2007.

[81] S. M. Danner, U. S. Hofstoetter, J. Ladenbauer, F. Rattay, and K. Minassian, "Can the human lumbar posterior columns be stimulated by transcutaneous spinal cord stimulation? a modeling study," *Artificial organs*, vol. 35, no. 3, pp. 257–262, 2011.

[82] N. I. Krouchev, S. M. Danner, A. Vinet, F. Rattay, and M. Sawan, "Energy-optimal electrical-stimulation pulses shaped by the least-action principle," *PLoS One*, vol. 9, no. 3, p. e90480, 2014.

[83] M. N. Ab Wahab, S. Nefti-Meziani, and A. Atyabi, "A comprehensive review of swarm optimization algorithms," *PLoS One*, vol. 10, no. 5, p. e0122827, 2015.

[84] J. Vesterstrom and R. Thomsen, "A comparative study of differential evolution, particle swarm optimization, and evolutionary algorithms on numerical benchmark problems.," in *IEEE Congress on Evolutionary Computation*, vol. 2, pp. 1980–1987, 2004.

[85] P. Civicioglu and E. Besdok, "A conceptual comparison of the cuckoo-search, particle swarm optimization, differential evolution and artificial bee colony algorithms," *Artificial intelligence review*, vol. 39, no. 4, pp. 315–346, 2013.

[86] S. Das, A. Abraham, and A. Konar, "Particle swarm optimization and differential evolution algorithms: technical analysis, applications and hybridization perspectives," in *Advances of computational intelligence in industrial systems*, pp. 1–38, Springer, 2008.

[87] M. A. Panduro, C. A. Brizuela, L. I. Balderas, and D. A. Acosta, "A comparison of genetic algorithms, particle swarm optimization and the differential evolution method for the design of scannable circular antenna arrays," *Progress In Electromagnetics Research*, vol. 13, pp. 171–186, 2009.

[88] J. H. Holland, "Genetic algorithms," *Scientific american*, vol. 267, no. 1, pp. 66–73, 1992.

[89] E. Mezura-Montes, J. Velázquez-Reyes, and C. A. Coello Coello, "A comparative study of differential evolution variants for global optimization," in *Proceedings of the 8th annual conference on Genetic and evolutionary computation*, pp. 485–492, ACM, 2006.

[90] S. Das and P. N. Suganthan, "Differential evolution: a survey of the state-of-the-art," *IEEE transactions on evolutionary computation*, vol. 15, no. 1, pp. 4–31, 2011.

[91] J. A. Lima, N. Gracias, H. Pereira, and A. Rosa, "Fitness function design for genetic algorithms in cost evaluation based problems," in *Evolutionary Computation, 1996., Proceedings of IEEE International Conference on*, pp. 207–212, IEEE, 1996.

[92] V. Feoktistov and S. Janaqi, "Generalization of the strategies in differential evolution," in *Parallel and Distributed Processing Symposium, 2004. Proceedings. 18th International*, p. 165, IEEE, 2004.

[93] R. Storn and K. Price, "Differential evolution–a simple and efficient heuristic for global optimization over continuous spaces," *Journal of global optimization*, vol. 11, no. 4, pp. 341–359, 1997.

[94] A. K. Qin, V. L. Huang, and P. N. Suganthan, "Differential evolution algorithm with strategy adaptation for global numerical optimization," *IEEE transactions on Evolutionary Computation*, vol. 13, no. 2, pp. 398–417, 2009.

[95] M. M. Ali and A. Törn, "Population set-based global optimization algorithms: some modifications and numerical studies," *Computers & Operations Research*, vol. 31, no. 10, pp. 1703–1725, 2004.

[96] E. Mezura-Montes and A. G. Palomeque-Ortiz, "Parameter control in differential evolution for constrained optimization," in *Evolutionary Computation, 2009. CEC'09. IEEE Congress on*, pp. 1375–1382, IEEE, 2009.

[97] R. S. Sankar, P. Asokan, R. Saravanan, S. Kumanan, and G. Prabhaharan, "Selection of machining parameters for constrained machining problem using evolutionary computation," *The International Journal of Advanced Manufacturing Technology*, vol. 32, no. 9-10, pp. 892–901, 2007.

[98] J. K. Trevathan, A. Yousefi, H. O. Park, J. J. Bartoletta, K. A. Ludwig, K. H. Lee, and J. L. Lujan, "Computational modeling of neurotransmitter release evoked by electrical stimulation: nonlinear approaches to predicting stimulation-evoked dopamine release," *ACS chemical neuroscience*, vol. 8, no. 2, pp. 394–410, 2017.

[99] Y. Jin, "A comprehensive survey of fitness approximation in evolutionary computation," *Soft computing*, vol. 9, no. 1, pp. 3–12, 2005.

[100] L. Geretti and A. Abramo, "The synthesis of a stochastic artificial neural network application using a genetic algorithm approach," in *Advances in imaging and electron physics*, vol. 168, pp. 1–63, Elsevier, 2011.

A

PYTHON CODE

Listing A.1: OPTIMIZE.py: Optimization file running the DE algorithm, the ETI model and interfasing with the MRG model in NEURON

```
# General
import getopt
import time
import numpy as np
#Signal
from scipy import signal
from scipy.interpolate import interp1d
import colorednoise as cn
#HELPER FUNCTIONS
from HELPER_FUNCTIONS import *
#MRG Model
from MRG_MODEL import *
#Optimization
import random
from deap import base
from deap import creator
from deap import tools
from deap import algorithms
#Parallel computing
from joblib import Parallel, delayed
import multiprocessing
from scoop import futures
#File system
import sys
import socket
import os
from os import path
from os.path import dirname, abspath
import math
import cmath
from scipy.fftpack import fft, ifft
#Settings
import settings as s
```

A

```
# File names
filename=""
opt_pars=s.OPT_PARS

def update_filename():
    global filename
    currentfolder=dirname(abspath(__file__))
    currentfoldername=os.path.basename(currentfolder)
    parentfolder= dirname(currentfolder)
    resultsfolder=parentfolder+"/RESULTS"
    if not os.path.exists(resultsfolder):
        os.mkdir(resultsfolder)
    index = 0
    while os.path.exists(resultsfolder+("/%s_"% index)+currentfoldername+".pkl"):
        index += 1
    filename=resultsfolder+("/%s_"% index)+currentfoldername+".pkl"

# SET UP DEAP FITNESS, INDIVIDUAL AND POPULATION
creator.create("FitnessMax", base.Fitness, weights=(1.0,)) #np.finfo(float).eps
creator.create("Individual", list, fitness=creator.FitnessMax, sim_results=None,
                                generations=list())

toolbox = base.Toolbox()
toolbox.register("attr_f", random.uniform, s.F_MIN, s.F_MAX)
toolbox.register("attr_a", random.uniform, s.A_MIN, s.A_MAX)
toolbox.register("attr_p_ratio", random.uniform, s.P_RATIO_MIN, s.P_RATIO_MAX)
toolbox.register("attr_imbalance", random.uniform, s.IMBALANCE_MIN, s.IMBALANCE_MAX)
toolbox.register("attr_ip_delay", random.uniform, s.IP_MIN, s.IP_MAX)
toolbox.register("attr_noise_ratio", random.uniform, s.NOISE_RATIO_MIN, s.NOISE_RATIO_MAX)
toolbox.register("attr_beta", random.uniform, s.NOISE_EXP_MIN, s.NOISE_EXP_MAX)
toolbox.register("attr_opt_CR", random.uniform, s.OPT_CR_MIN, s.OPT_CR_MAX)
toolbox.register("attr_opt_F", random.uniform, s.OPT_F_MIN, s.OPT_F_MAX)
toolbox.register("attr_elem", random.uniform, s.ELEM_MIN, s.ELEM_MAX)

attributes=[toolbox.attr_f, toolbox.attr_a, toolbox.attr_p_ratio,
        toolbox.attr_imbalance,toolbox.attr_ip_delay,toolbox.attr_ip_delay,
        toolbox.attr_noise_ratio,toolbox.attr_beta,toolbox.attr_opt_CR,toolbox.attr_opt_F]

for i in range(s.N_CATHODIC+s.N_ANODIC):
    attributes.append(toolbox.attr_elem)
attributes=tuple(attributes)

toolbox.register("individual", tools.initCycle, creator.Individual, attributes, 1)
toolbox.register("population", tools.initRepeat, list, toolbox.individual)

# MAIN
def main():
    update_filename()
    run_optimization()

# RUN OPTIMIZATION FUNCTION
def run_optimization():
    # 1. SETUP POPULATION AND PARALLEL PROGRAMMING ENVIRONMENT

    pop = toolbox.population(n=s.POP_SIZE)
    num_cores = multiprocessing.cpu_count()
```

```
if s.CORES == -1:
    num_used_cores = num_cores / 2
else:
    num_used_cores = s.CORES
pool = multiprocessing.Pool(num_used_cores)
toolbox.register("map", pool.map)
# II. SETUP RECORDING VARIABLES
hof = tools.HallOfFame(s.HOF_SIZE)

stats = tools.Statistics(key=lambda ind: ind.fitness.values)
stats.register("avg", np.mean, axis=0)
stats.register("std", np.std, axis=0)
stats.register("min", np.min, axis=0)
stats.register("max", np.max, axis=0)
logbook = tools.Logbook()
logbook.header = "gen", "evals", "t", "avg", "min", "max", "std"

# III. EXECUTE DIFFERENTIAL EVOLUTION ALGORITHM

# 0. Evaluate generation 0
t_start = time.time()

results = list(toolbox.map(run_model, zip(pop,np.ones(len(pop))*float(s.fitness_function),
                           np.ones(len(pop))*0.0,np.ones(len(pop))*0.0)))
for ind, res in zip(pop, results):
    ind.fitness.values = res['fitness']
    ind.sim_results = res['sim_results']
    ind.generations=[0]
# Record Data (Gen 0)
hof.update(pop)

record = stats.compile(pop)
logbook.record(gen=0, evals=len(pop),t=time.time()-t_start,
                           t_total=time.time()-t_start, **record)
print(logbook.stream)

# Begin the evolution
g=1
longest_g=0
while g<s.GENERATIONS and (time.time()-t_start)<s.MAX_TIME-longest_g*3:

    t_start_g = time.time()
    # 1. Generate next population by differential evolution
    new_pop = toolbox.clone(pop)
    [a] = tools.selBest(pop,1)
    for k, agent in enumerate(pop):
        [b, c] = tools.selRandom(pop,2)
        index = random.randrange(s.N_CATHODIC+s.N_ANODIC+s.N_PARAMETERS)
        CR = pop[k][9]
        F = pop[k][10]
        for i, value in enumerate(agent):
            if i == index or random.random() < CR:
                new_pop[k][i] = a[i] + F * (b[i] - c[i])
        limit_individual(new_pop[k])
    # 2. Evaluate next population
    only_eti = 1.0 * (g > s.NO_MODEL_START_GEN and
                           (g-s.NO_MODEL_START_GEN) % s.COMPLETE_MODEL_EVERY != 0)
```

A

```
        results = list(toolbox.map(run_model, zip(new_pop, np.ones(len(new_pop))
                                        *float(s.fitness_function),np.ones(len(new_pop))*0.0,
                                        np.ones(len(new_pop))*only_eti)))
        for ind, res in zip(new_pop, results):
            ind.fitness.values = res['fitness']
            ind.sim_results = res['sim_results']
            ind.generations = [g]

        # 3. Keep the best between parent and child
        evals = 0
        k_elites = int(np.ceil(s.ELITISM * s.POP_SIZE))
        elite = tools.selBest(pop, k_elites)
        rest = tools.selWorst(pop, s.POP_SIZE - k_elites)
        normal = tools.selBest(rest, s.POP_SIZE - 2 * k_elites)
        worst = tools.selWorst(rest, k_elites)
        for k, agent in enumerate(pop):
            if agent in normal and new_pop[k].fitness > pop[k].fitness:
                pop[k] = new_pop[k]
                evals = evals + 1
        new_pop_elite = toolbox.clone(elite)
        i = 0
        for k, agent in enumerate(pop):
            if agent in elite and i < k_elites:
                new_pop_elite[i] = new_pop[k]
                i = i + 1
        new_pop_elite = toolbox.clone(elite)
        i = 0
        for k, agent in enumerate(pop):
            if agent in worst:
                if new_pop[k].fitness > pop[k].fitness:
                    pop[k] = new_pop[k]
                    evals = evals + 1
                if i < k_elites:
                    if new_pop_elite[i].fitness > pop[k].fitness:
                        pop[k] = new_pop_elite[i]
                        evals = evals + 1
                i = i + 1

        # Record Data
        hof.update(pop)
        record = stats.compile(pop)
        longest_g=max(longest_g,time.time() - t_start_g)
        logbook.record(gen=g,pop=len(pop), evals=evals,t=time.time() - t_start_g,
                                        t_total=time.time() - t_start, **record)
        print(logbook.stream)

        # Variable pattern
        if s.DOUBLING_EVERY != 0:
            if g % s.DOUBLING_EVERY == 0:
                for ind in pop:
                    ind.extend(ind[s.N_PARAMETERS:])

        g=g+1

    #Get simulation results from hall of fame
    results = list(toolbox.map(run_model, zip(hof, np.ones(len(hof))
                                * float(s.fitness_function),
```

```
                                    np.ones(len(hof)) * 1.0,np.ones(len(hof)) * 0.0)))
    for ind, res in zip(hof, results):
        ind.sim_results = res['sim_results']

    #Store data
    par, recpar = readConfigurations("model.cfg")
    store_data(filename,[hof,logbook,opt_pars,par,recpar])
    return (hof, hist, logbook, pf)

# RUN MODEL FUNCTIONS
def run_model(input):
    # READ CONFIG
    verbose = False
    par, recpar = readConfigurations("model.cfg")
    individual = input[0]
    fitness_function = input[1]
    return_simulation_data = input[2]
    only_eti = input[3]

    # GENERATE WAVEFORM
    (t, i) = individual_to_waveform(individual, par['tstop'])

    # EVALUATE NEURON MODEL
    sim_results = {}
    if not only_eti:
        # SETUP NEURON MODEL
        createMRGaxon(par, verbose)
        rec = recordMRGaxon(recpar, verbose)
        resetRecorder(rec, False)
        updateMRGaxon(par, False)
        # RUN NEURON SIMULATION
        runMRGaxon(rec, t, i)
        # EVALUATE EFFICACY OF HFB
        lastNodeName = 'spk' + str(np.max(int(par['axonnodes'] - 1)))
        spks = np.array(rec['spiketimes'][lastNodeName])
        blocked = len(spks[(spks > 10.0) & (spks < 20.0)]) == 0
        onset_spikes = len(spks[(spks > 0.0) & (spks < 10.0)])
        repetitive_firing = len(spks[(spks > 0.0) & (spks < 20.0)]) > 2

        # DOWNSAMPLE RESULTS
        sim_results['voltage'] = {}
        for k, x in rec['voltage'].iteritems():
            y = list(x)
            sim_results['voltage'][k] = y[::100]
        sim_results['i_block'] = {}
        for k, x in rec['i_block'].iteritems():
            y = list(x)
            sim_results['i_block'][k] = y  # y[::10]
    else:
        blocked = True
        onset_spikes = 2
        repetitive_firing = False
    # EVALUATE ETI MODEL
    sim_results.update(simulate_ETI(t, i))
    q_rct = abs(sim_results['ETI_results']['q_rct'])
    q_zw = abs(sim_results['ETI_results']['q_zw'])
    faradaic_charge = max(abs(q_rct + q_zw))
```

A

```
v_total = abs(sim_results['ETI_results']['v_total'])
v_cpa = sim_results['ETI_results']['v_cpa']
v_rms = np.sqrt(np.mean(v_cpa ** 2))

energy_consumption = (t[1] - t[0]) * sum((np.array(i) * 1e-3) ** 2)
charge_injection_mismatch = abs(sum(i) ** 2) + np.finfo(float).eps

# Store results
sim_results.update({'single': {'v_rms': v_rms, 'faradaic_charge': faradaic_charge,
            'blocked': blocked, 'onset_spikes': onset_spikes,
            'repetitive_firing': bool(repetitive_firing),
            'energy_consumption': energy_consumption, 'max_veti': max(v_cpa),
            'min_veti': min(v_cpa),
            'charge_injection_mismatch': charge_injection_mismatch}})

if not return_simulation_data:
    sim_results = {}

# Determine fitness
if fitness_function == 0:
    fitness = (100 * blocked - 200000 * faradaic_charge,)
if fitness_function == 1:
    fitness = (100 * blocked - 50 * v_rms,)
if fitness_function == 2:
    fitness = (100 * blocked - 20000 * charge_injection_mismatch,)
if fitness_function == 3:
    val = 100 * blocked
    if max(v_cpa) > 0.9 or max(v_cpa) < -0.6:
        val = val - 40
    else:
        val = val + (0.9 - max(v_cpa)) * 10
    if min(v_cpa) > 0.9 or min(v_cpa) < -0.6:
        val = val - 40
    else:
        val = val + (min(v_cpa) - 0.6) * 10
    fitness = (val,)
if fitness_function == 4:
    val = 100 * blocked
    window_max = 0.9
    window_min = -0.6
    max_v = max(v_cpa)
    min_v = min(v_cpa)
    # Inside of the window
    if max_v <= window_max and min_v >= window_min:
        margin = (window_max - max_v) + (min_v - window_min)
        val = val + 50 * margin / (window_max - window_min)
    # Both Outside of the window (same side) (offset too big)
    if min_v > window_max:
        distance = (max_v - window_max)
        val = val - 50 * distance / (window_max - window_min)
    if max_v < window_min:
        distance = (window_min - min_v)
        val = val - 50 * distance / (window_max - window_min)
    # Both outside of the window (different side) (amplitude too big)
    if max_v > window_max or min_v < window_min:
        if min_v > window_min:
            min_v = window_min
```

```
            if max_v < window_max:
                max_v = window_max
            distance = (window_min - min_v) + (max_v - window_max)
            val = val - 50 * distance / (window_max - window_min)
        fitness = (val,)
    if fitness_function == 5:
        val = 100 * blocked
        window_max = 0.9
        window_min = -0.6
        max_v = max(v_cpa)
        min_v = min(v_cpa)
        distance = abs(window_min - min_v) + abs(window_max - max_v)
        val = val - distance * 50 / (window_max - window_min)
        fitness = (val,)
    if fitness_function == 6:
        fitness = (100 * blocked - 10 * onset_spikes,)
    if fitness_function == 7:
        fitness = (100 * blocked - 100000 * energy_consumption,)
    if fitness_function == 8:
        v_safe = 0.15
        fitness = (100 * blocked - 50 * (abs(max(v_cpa) - v_safe) + abs(min(v_cpa) - v_safe)),)
    if fitness_function == 9:
        v_safe = 0.15
        fitness = (100 * np.exp(-0.2 * (abs(max(v_cpa) - v_safe) + abs(min(v_cpa) - v_safe)))
                                - 100 * (1 - 1 * blocked),)
    if fitness_function == 10:
        v_safe = 0.15
        fitness = (100 * np.exp(-(abs(max(v_cpa) - v_safe) + abs(min(v_cpa) - v_safe)))
                                - 100 * (1 - 1 * blocked),)

    return {'fitness': fitness, 'sim_results': sim_results}

if __name__ == '__main__':
    main()
```

Listing A.2: settings.py: Optimization settings file

```
import numpy as np

MAX_TIME=5*60#s
POP_SIZE, GENERATIONS =1, 1
CORES = 2 #-1 implies half of the available cores
N_CATHODIC=50
N_ANODIC=50
HOF_SIZE = 20
CHECKPOINTS = 2
# Differential evolution parameters
CR = 0.8
F = 1

# Configuration
F_MIN, F_MAX = 5.0, 5.0 #kHz
A_MIN, A_MAX = 2.0, 2.0 #mA
P_RATIO_MIN, P_RATIO_MAX = 0.5, 0.5
IMBALANCE_MIN, IMBALANCE_MAX = 1.0, 1.0
IP_MIN, IP_MAX = 0.0,0.0
```

A

```
NOISE_RATIO_MIN, NOISE_RATIO_MAX = 1.0, 1.0
NOISE_EXP_MIN, NOISE_EXP_MAX = 1.0, 1.0
OPT_CR_MIN,OPT_CR_MAX = 0.8, 0.8
OPT_F_MIN,OPT_F_MAX = 1.0, 1.0
ELEM_MIN, ELEM_MAX = 0.0, 0.0

SHAPE=0 # 0: Arbitrary, -1: Cathodic & Anodic, -2: Anodic & Cathodic, 1: Squarewave,
                        2: Sinewave, 3: Ramp
CHARGE_BALANCE= False
ELITISM= 0.1
DOUBLING_EVERY = 0 # 0: No variable pattern. Double pattern every DOUBLING_EVERY
NO_MODEL_START_GEN= 0 #-1: Run complete model always,
COMPLETE_MODEL_EVERY=1 # Check model
fitness_function=10


VALUES=[5.0]
INDEX=0

VERBOSE=False
```

Listing A.3: HELPERFUNCTIONS.py

```
# General
import getopt
import time
import numpy as np
#Signal
from scipy import signal
from scipy.interpolate import interp1d
import colorednoise as cn
#Settings
import settings as s

#HELPER FUNCTIONS
noise = cn.powerlaw_psd_gaussian(1, 100)
noise = noise / max(noise)

def store_data(filename,data):
    import pickle
    with open(filename, 'wb') as f:
        pickle.dump(data, f,protocol=-1)
def load_data(filename):
    import pickle
    with open(filename,'rb') as f:  # Python 3: open(..., 'rb')
        hof, hist, logbook, pf = pickle.load(f)
    return (hof,hist,logbook,pf)
def limit_individual(individual):
    for i,v in enumerate(individual):
        if i<len(s.MINS):
            if v<s.MINS[i]:
                individual[i] = s.MINS[i]
            if v>s.MAXS[i]:
                individual[i] = s.MAXS[i]
        else:
            if v<s.MINS[len(s.MINS)-1]:
```

```
                individual[i] = s.MINS[len(s.MINS)-1]
            if v>s.MAXS[len(s.MINS)-1]:
                individual[i] = s.MAXS[len(s.MINS)-1]

def individual_to_waveform(individual,t_stop):
    #Get Parameters
    f=individual[0]
    a=individual[1]
    phase_ratio=individual[2]
    desired_charge_imbalance_ratio=individual[3]
    ip_1=individual[4]
    ip_2 = individual[5]
    noise_factor=individual[6]
    beta_noise = individual[7]
    a_noise=a*noise_factor

    #Calculate periods
    T = 1 / f
    T_ip_1 = ip_1*T
    T_ip_2 = ip_2*T
    T_remaining=T-T_ip_1-T_ip_2
    T_1 = phase_ratio * T_remaining
    T_2 = (1 - phase_ratio) * T_remaining

    # Determine shape
    if s.SHAPE == 0: #Arbitrary
        shape_1 = np.concatenate([individual[s.N_PARAMETERS:s.N_CATHODIC + s.N_PARAMETERS]])
        shape_2 = np.concatenate([individual[s.N_CATHODIC + s.N_PARAMETERS:
                    s.N_CATHODIC + s.N_ANODIC + s.N_PARAMETERS]])
    if s.SHAPE == -1: #Cathodic & Anodic
        shape_1 = np.concatenate([[i*(-1) for i in individual[s.N_PARAMETERS:
                    s.N_CATHODIC+s.N_PARAMETERS]]])
        shape_2 = np.concatenate([individual[s.N_CATHODIC+s.N_PARAMETERS:
                    s.N_CATHODIC+s.N_ANODIC+s.N_PARAMETERS]])
    if s.SHAPE == -2: #Anodic & Cathodic
        shape_1 = np.concatenate([individual[s.N_CATHODIC+s.N_PARAMETERS:
                    s.N_CATHODIC+s.N_ANODIC+s.N_PARAMETERS]])
        shape_2 = np.concatenate([[i*(-1) for i in individual[s.N_PARAMETERS:
                    s.N_CATHODIC+s.N_PARAMETERS]]])
    if s.SHAPE==1: #Squarewave
        shape_1 = np.concatenate([np.sin(np.linspace(0,np.pi,s.N_CATHODIC))*(-1)])
        shape_2 = np.concatenate([np.sin(np.linspace(0,np.pi,s.N_ANODIC))])
    if s.SHAPE==2: #Sinewave
        shape_1 = np.concatenate([np.ones(s.N_CATHODIC)*(-1)])
        shape_2 = np.concatenate([np.ones(s.N_ANODIC)])
    if s.SHAPE == 3: #Ramp
        shape_1 = np.concatenate([np.linspace(0,-1,s.N_CATHODIC)])
        shape_2 = np.concatenate([np.linspace(1,0,s.N_CATHODIC)])

    # Noise addition
    if noise_factor != 0:
        shape_1 = shape_1 + a_noise * noise[:len(shape_1)]
        shape_2 = shape_2 + a_noise * noise[len(shape_2):]

    #Reconstruct period
    shape_ip=np.zeros(50)
    shape_period = np.concatenate([shape_1, shape_ip, shape_2, shape_ip])
```

```
    t_steps_1 = np.ones(len(shape_1)) * T_1 / (len(shape_1))
    t_steps_2 = np.ones(len(shape_2)) * T_2 / (len(shape_2))
    t_steps_ip_1 = np.ones(len(shape_ip)) * T_ip_1 / len(shape_ip)
    t_steps_ip_2 = np.ones(len(shape_ip)) * T_ip_2 / len(shape_ip)
    t_steps_period = np.concatenate([t_steps_1, t_steps_ip_1, t_steps_2, t_steps_ip_2])



    #Reconstruct waveform
    periods = int(np.ceil(t_stop * f))
    i = np.concatenate([[0], np.tile(shape_period, periods)])
    t_steps = np.tile(t_steps_period, periods)
    t = [round(elem, 9) for elem in np.concatenate([[0], np.cumsum(t_steps)])]



    #Oversample
    over_sample = interp1d(t, i)
    t_os = np.linspace(max(min(t), 0), min(max(t), t_stop), len(i) * 10)
    i_os = a*over_sample(t_os)


    #Charge balance
    if s.CHARGE_BALANCE:
        i_os_plus = np.clip(i_os, 0, max(i_os))
        i_os_minus = np.clip(i_os, min(i_os), 0)
        if sum(i_os_plus) != 0 and sum(i_os_minus) != 0:
            charge_imbalance_ratio = desired_charge_imbalance_ratio
                        * (-sum(i_os_minus) / sum(i_os_plus))
            if charge_imbalance_ratio < 1:
                i_os_plus = [elem * charge_imbalance_ratio for elem in i_os_plus]
            else:
                i_os_minus = [elem / charge_imbalance_ratio for elem in i_os_minus]
        i_os = i_os_plus + i_os_minus

    return (t_os, i_os)
```